Solving Series Resistance Problems In GaSb Thermophotovoltaics with Graphene and Other Approaches

Benjamin Conlon

Thesis submitted to the faculty of the Virginia Polytechnic Institute and State University in partial fulfillment of the requirements for the degree of

Master of Science
In
Electrical Engineering

Luke F Lester
Xiaoting Jia
Wei Zhou

4/28/17
Blacksburg, VA

Keywords: Photovoltaics, GaSb, Graphene, Thermophotovoltaics

ABSTRACT Academic

Solving Series Resistance Problems In GaSb ThermoPhotovoltaics with Graphene and Other Approaches

Benjamin Conlon

GaSb Thermophotovoltaics are a key technology in the search for the ability to power small scale autonomous systems. In this work, MBE grown GaSb photovoltaic devices are fabricated and tested under AM 1.5 conditions. These devices displayed short circuit current values as high as 40 mA/cm^2 but were found to have poor series resistance. The parasitic resistive characteristics were factored out of the measured cell data and it was found that the photocurrent for the fabricated devices could be as much as 6 mA/cm^2 higher then the measured short circuit current. An additional layer of metal was added to the reduce the deleterious resistance characteristics, and it was found to lower the series resistance down to a 4 Ω average across almost all of the devices. The average J_{SC} for all of these devices increased to over 30 mA/cm^2, with highs well over 40 mA/cm^2, a more consistent result than the original single metal deposition devices. Graphene was applied to the originally fabricated devices in an attempt to remove the series resistances issues as well as act as a surface passivation layer. The graphene was able to reduce series resistance by as much as 50% on some of the devices, with a corresponding 6 mA/cm^2 increase in short circuit current exhibited. The photocurrent and diode current values were not changed by more than a measurement error, an indication that surface passivaiton may not have taken place. Graphene was a suitable approach for solving the series resistance issue and its use as both a transparent conductive layer and surface passivation material deserve further investigation.

ABSTRACT General Audience

Solving Series Resistance Problems In GaSb ThermoPhotovoltaics with Graphene and Other Approaches

Benjamin Conlon

Photovoltaics are a technology which have the potential to solve the energy crisis which plagues the world. Though silicon solar cell technologies have effeciencies which can capture large quantities of light and turn it into usable electric energy, they are not able to capture all the usable wavelengths of light which strike the earths surface. Materials like GaSb are able to capture different wavelength of light than silicon, including infrared radiation generated through an open flame or industrial processes. Though it possesses outstanding potential as an electrical generator, GaSb is a new material which scientists and engineers are seeking to understand an implement. In this work, we utilize graphene to solve some of the inherent problems with the GaSb material structure. Graphenes large electrical and thermal conduction properties as well as it's near constant transparency across all wavelengths of light make it ideal for thermal photovoltaic applications. In this work we transfer a layer of graphene onto alread fabricated GaSb Thermophotovoltaic devices. These devices display improvement in the resistive characteristics of each cell as well as it's overall effeciency.

Dedication

This work is dedicated to my parents (Sean and Fredda) as well as my sister (Molly). Without them I would have never started or finished this journey. This work is also dedicated to the planet, because people tend to forget about it and I will not one of the ones who does.

Acknowledgements

I would like to thank Dr. Luke Lester for his help in developing and executing the work in this thesis. Without the opportunity he gave me to get my master's I would not be where I am today. It has been a pleasure to work with you on this research as well as be an aid in helping to get the 4805/06 class to where it is today. Thank you for all your time and encouragement.

I would like to thank Drs. Xiaoting Jia and Wei Zhou for their insight and ideas. Working with them in my capacity as a TA for the 4805/06 class has been both instructional and enjoyable. I thank them for being on my committee and inspiring me to be able to think through problems in unique and inventive ways.

I would like to thank Daniel Herrera for being a wonderful lab mate and someone I can always bounce ideas off of. You have helped me to complete my work and I know I would not be here today without your friendship and support.

I would like to thank Shaimaa Abdullah for being a kind face and a helpful editor in all of the work we have completed. It was always nice to know that you would be there if we had questions on any theoretical aspect of this work.

I would like to thank my family, who know how much they mean to me and would have supported me whether I finished this degree or not. I hope that I can repay you for all that you've given me.

I would especially like to thank George Rai and Sarat Saluru for dealing with me for the past 9 months. Good luck on your own work and I can't wait to do nothing for a few days with the both of you.

I would like to thank the friends I came with to graduate school and those I've gained along the way. I would not be here if not for them and I would never have enjoyed myself as much.

I would especially like to thank two of these friends, Cypress Beach and Benjamin Jaqcues. You have been one of the few things I am truly thankful for in this whole experience. I will never be able to express my gratitude for how much you helped me to complete this degree.

I would like to thank my Sifu Herbie Holland. You kept me balanced in the two years I've been in graduate school, and the three years I've known you before this. I will cherish what I've learned from you and hope to be able to spread my knowledge to people in the future.

And thank you to the planet because your awesome and I hope we stay friends for as long as I'm around.

Table of Contents

ABSTRACT Academic ii

ABSTRACT General Audience iii

Dedication iv

Acknowledgements v

Chapter 1: Introduction to Photovoltaics and Graphene 1

Solar Cell Development 1

Solar Cell Limitations 3

GaSb Photovoltaics 5

Solar Cell Operation 6

Graphene Background 10

Theoretical Graphene mobility 10

Phonon transport 12

Non Theoretical mobility 13

Exfoliated graphene mobility 14

CVD Grown graphene 17

Graphene & GaSb 18

Chapter 2: Fabrication and Optimization of PV Devices 19

Fabrication: 19

Back Metal Contact 20

Front Metal Deposition 21

Shading Loss Prevention 22

Optimized Cell Designs 28

Cell Characteristics 30

2^{nd} metallization 33

Chapter 3. GaSb Parameter Extraction & Graphene Analysis 35

Diode Equation Basics 35

Circuit analysis 36

I_0 and I_{Ph} Extraction 39

2D Material Solution to the Series Resistance 40

Graphene Transfer Process 41

Transfer Method A 42

Transfer Method B: 43

Graphene on TPV 43

V_{OC} & I_0 changes 44

Characteristic Resistances 45

Effect of graphene coating on J_{SC} & J_{PH} 45

Chapter 4: Conclusion and Future work 48

Conclusions on the GaSb Parasitic Resistance Problem 48

Blackbody Cell Measurements 49

Full Graphene Front Contacts 50

Etching of Graphene Using CO_2 50

References 52

Appendix A: RTA Chart **55**
Appendix B: Full results **56**
Appendix C: PV Characteristics Derivation **57**

Chapter 1: Introduction to Photovoltaics and Graphene

Solar Cell Development

Electricity drives the world in which we live in, and it is inescapable in this globally connected society. The ability to generate electricity cleanly and store it may well be the challenge that drives humanity in the 21st century. Currently, a majority of the world's population uses fossil fuels to generate the electricity used in their daily lives. These fuels are portable, energy dense, and whose extraction and implementation has been optimized by years of research and investment. Though the infrastructure and implementation of fossil fuels is complete, years of research has shown that fossil fuels are bad for the environment and are a major contributor to global warming and climate change. Removing fossil fuels from the earth and refining them is also costly as chemicals used in these processes are toxic and can cause permanent environmental damage.

This technological revolution, powered by electricity, has enabled prosperity and health to grow for people all across the world. The advent of the cheap mobile smart phone has brought about a data explosion, and this exponential growth of data carries with it a corresponding need for energy creation. As world population is predicted to grow to 9.7 billion by 2050, this demand will increase faster than ever before as these people demand access to common utilities like clean water and internet access.[1] In order to make this exponential growth sustainable, the generation and storage of electricity must be performed in clean and reliable ways. These methods must be economically feasible, and not put a strain on infrastructure already in place at the

moment. There are many avenues in which this goal is being pursued, but one of the most promising ones from an energy generation standpoint are photovoltaics.

Photovoltaics are a device first discovered to be viable commercially in the late 1950's, but the science behind them has been known since 1839 when it was discovered by Edmond Becquerel.[2, 3] The first designed solar cells were made using selenium which intrinsically display photovoltaic effects. These cells were not able to generate meaningful amount of electricity from the light they were exposed to, and, thus, were not viable as a power source. This phenomenon though intriguing from a scientific perspective, was thought a mere oddity and not something which was viewed as a potential energy source. This changed when scientists at Bell labs discovered that the same silicon used in making microchips produced an electric charge when exposed to the sun.[4] These early solar cells were investigated and improved upon so as to bring their overall efficiency from 14% in 1975 to over 25% in 2015. [5] Semiconductor photovoltaics have evolved with the semiconductor industry, and today are one of the fastest growing forms of energy production in the world.

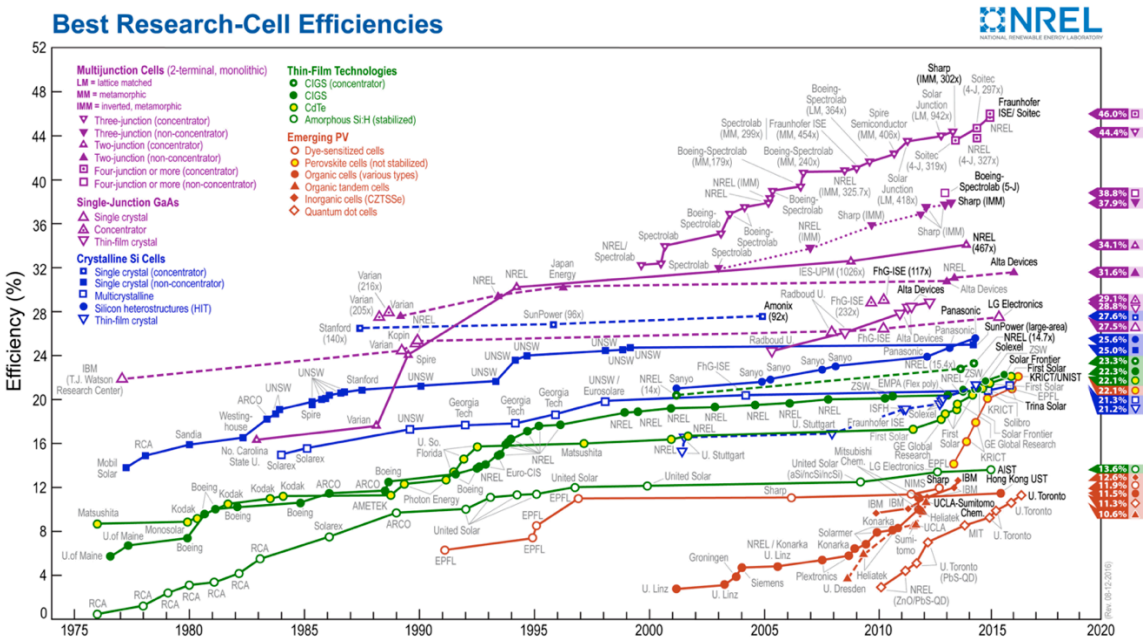

Figure 1: Technological roadmap of PV device efficiency and growth. [5,6]

Solar Cell Limitations

Though silicon has been the dominant technology for photovoltaics, it inherently has a limit to its efficiency. Although the bandgap of silicon is 1.1 eV, and tailored very well to the most energy dense part of the solar spectrum (green light), it does not have the ability to absorb efficiently beyond a wavelength of 1.1 µm. [7] These are parts of the electromagnetic spectrum, including waste heat, that bathe the earth and are produced in large amounts by industrial processes. It would be beneficial to be able to harness these wasted energies as electricity and make solar energy generation more efficient.

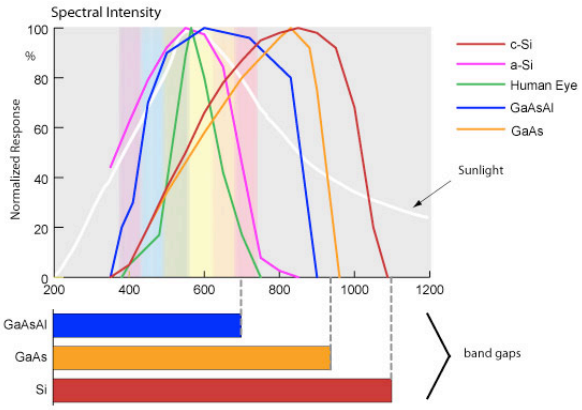

Figure 2: A Visual representation of how bandgap can influence the absorption spectrum. The materials with large bandgaps have smaller absorption windows. The peaks of these materials are not symmetrical, with max response values located at longer wavelengths. [8]

To resolve the bandgap limitations of conventional silicon, materials with different bandgaps such as GaAs and GaSb, are made into photovoltaics to capture as much of the electromagnetic spectrum as possible. GaSb fulfills a very particular set of the spectrum that is best for aspects of electromagnetic spectrum in the infrared and near infrared. It is of particular interest for small-scale autonomous vehicles, as shown in Figure 3. A GaSb thermophotovoltaic (TPV) is a good fit for the energy density requirements of these vehicles.

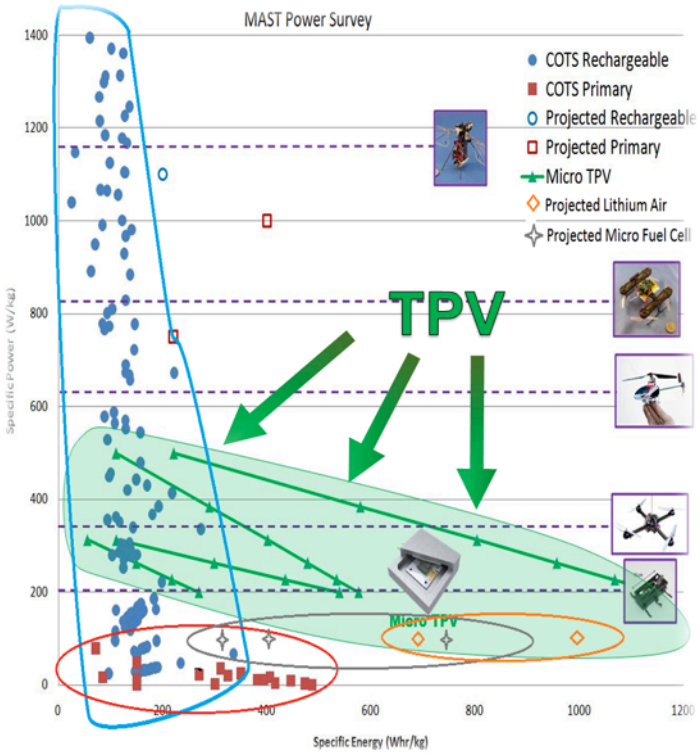

Figure 3: A map of energy requirements for various small scale autonomous systems. TPV's Fulfill the needs of Micro-Autonomous systems the most effectively of any proposed power systems. [9]

These GaSb-based systems exist in a TPV module exposed to a heat-generating flame mediated through a photonic crystal that re-shapes the emission spectrum. This flame generator can be on the scale of typical MEMs devices, and made of a semi-conductor material.[10] The photonic crystal would act as a spectrum shaper, and transmit wavelengths of light which the GaSb TPV can absorb efficiently. This system would allow for small-scale autonomous systems to be powered on board inexpensively, with only small amounts of fuel necessary. Advancements in GaSb photovoltaics can enable these technologies that directly convert combustion to electricity with no moving parts to reach fruition.

GaSb Photovoltaics

GaSb is a material which is in no way as mature as Silicon or GaAs in terms of fabrication capabilities and experience. Discovered in 1926, it has been used in infrared LED's and photodiodes, as well as lasers due to its ability to detect and emit wavelengths in the infrared range. It has a bandgap of 0.72 eV that is substantially lower than that of silicon, which though not perfect for solar energy collection, is tuned to collecting blackbody radiation from a thermal source at 900 K.[11] It's use in photovoltaics is newer, and as such is a field which stands to make substantial contributions to the field. GaSb displays good electron transport mobility (>1,000 cm2/V-s), but it's hole mobility is substantially less than that of GaAs and Si (<875 cm^2/V-s).[12] GaSb as a compound does not occur readily in nature, and must be created under fixed conditions in semi-conductor growth processes. To understand how GaSb can be utilized in photovoltaic applications, first photovoltaic device operation must be understood.

Solar Cell Operation

A solar cell made from a semiconductor in its simplest form consists of a PN junction where the P-side has a majority of positive charge carriers, and the N-side has a majority negative charge carriers. These carriers are created by dopant atoms such as Tellurium (n-type dopant in GaSb) and Beryllium (p-type dopant in GaSb). The difference in the chemical potential of these positive and negative sides causes a built-in electric field to occur, which then separates and transports excess electron-hole pairs that are generated by incident light to electrical terminals before they recombine. The amount of these charges collected over time is represented as the current generated by the solar cell. The behavior of the cell is usually measured by conducting a test in a solar simulator, where the cell is exposed to artificial sunlight while the voltage is varied from

zero to a positive voltage. The intersection on both the current and voltage axis are important points for photovoltaics. Short circuit current (I_{SC}) is the intersection of the cell behavior along the current axis and it represents the highest usable current value achieved by the device. The open circuit voltage (V_{OC}) represents the highest usable voltage value exhibited by the cell.

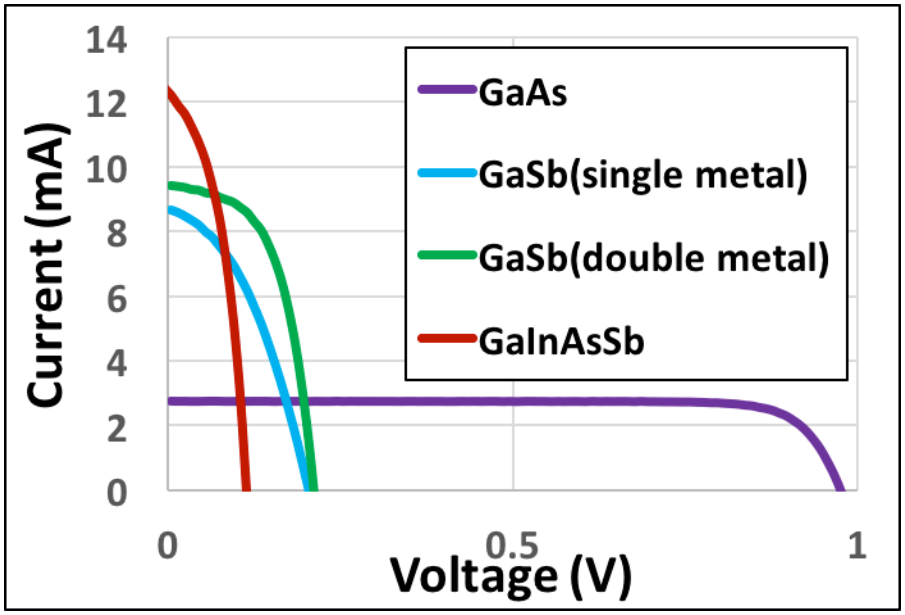

Figure 4: Current vs. Voltage relationships for each type of cell fabricated for the work in this project under AM 1.5 conditions. The GaAs displayed the lowest current generation, but exhibited voltage values large enough to offset this. The GaSb cells showed remarkably different behavior from one to two metallization steps, the effect of improved resistance characteristics. The GaInAsSb had the poorest efficiency response to the AM1.5 conditions, but this was to be expected as it's bandgap is more suited to TPV applications than pure solar simulation.

The peak power of these cells is determined by the point on the IV curve exhibited in Figure 4 where the highest voltage-current value combination is achieved. A useful measurement tool for cell behavior can be drawn by comparing the ideal peak power point, which is a theoretical point of where V_{OC} and I_{SC} would meet if orthogonal lines were drawn to their intersection, with the measured peak power. This value is known as the fill factor, and it is a measure of the ideality of the cell in terms of both the

power generation capabilities as well as the design of the cells to minimize parasitic resistances.

Why do these devices not behave in an ideal fashion? The ideal diode behavior of the devices is disturbed by the resistances inherent to the photovoltaic device. The series resistance value is parasitic to the current of the device, and is estimated from the slope of the IV curve at $V=V_{oc}$. A large series resistance can actually degrade the short circuit current of the cell. Analogously, the shunt resistance is estimated from the slope of the IV curve at $I=I_{sc}$, and the shunt resistance can cause degradation in V_{oc}. However, even if there is no observable degradation in the I_{SC} and V_{OC} values from the parasitic series and shunt resistances, the fill factor can be deleteriously effected.

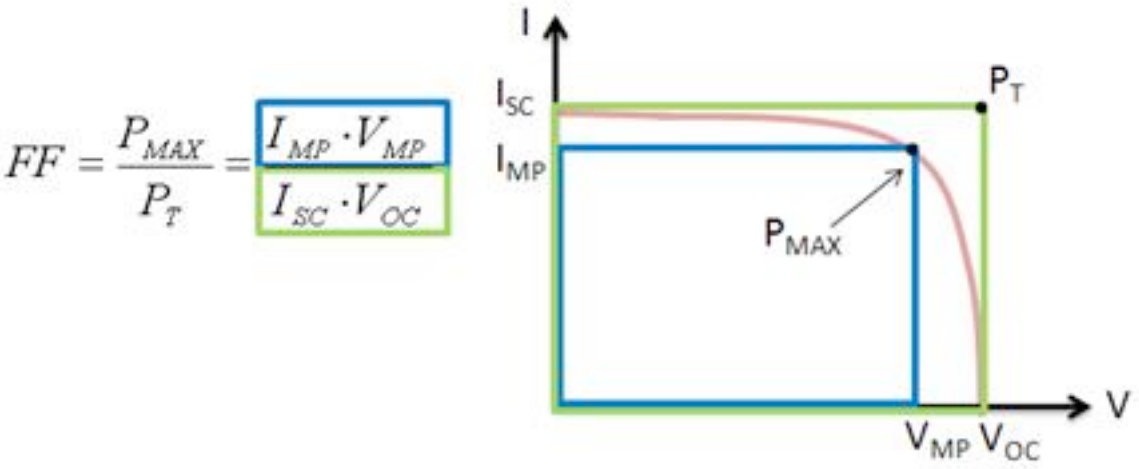

Figure 5: A visual representation of what constitutes fill factor for a photovoltaic when the IV characteristics are changed to quadrant I. It is a way of assessing how far away from ideal behavior a photovoltaic device is operating. The deviations for the cell exist because of poor shunt and series resistances in the device. [13]

It is easiest to see these resistances when the photovoltaic is visualized using a circuit diagram as shown in Figure 5. It is important to note that the measured current in the external circuit can be different that the photocurrent (I_{PH} or in Figure 5, I_L) because of the presence of R_S and R_P. The short circuit current, which is an extrinsic parameter, is commonly assumed to be the same I_{PH}, but for relatively immature materials technologies

such as GaSb or GaInAsSb (about 0.5 eV bandgap), this is not always the case. Calculating the exact series resistance and shunt resistances are vital to determining the I_{PH}, which is an intrinsic parameter.

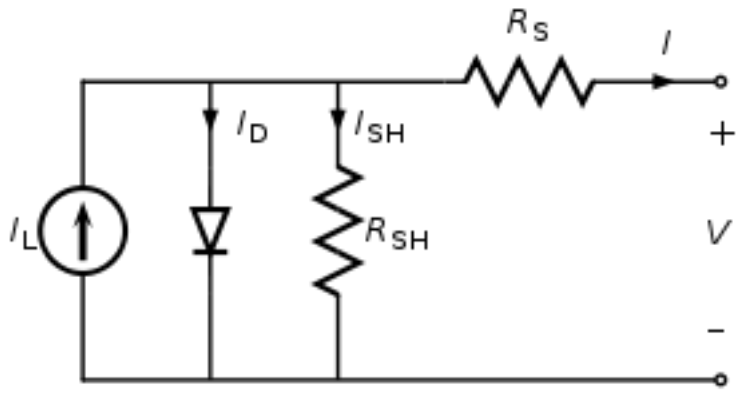

Figure 6: A photovoltaic device interpreted as a circuit. In most PV devices the shunt resistance (R_{SH} or R_P) is orders of magnitude larger than R_S. Later in this work, we see that when this is not the case, for all photovoltaic devices. [14]

To solve issues like series resistance there are a variety of approaches one can take. The front contact grid of a solar cell is part of the current collection mechanism of the device, and its design can have a profound impact on the behavior of a photovoltaic device. Most front contacts of a solar cell are made of metal, and as the contact grid cannot block all the light to the semi-conductor, the metal must be configured in such a way as to minimize its overall resistance. Many designs have been tried, but simple grid patterns are one of the most common as they are easy to evaluate and fabricate. An issue embedded in the grid network is that the sheet resistance of the semiconductor between the metal lines, dictated by the semi-conductor material and dopant concentration, must be optimized along with the grid pattern. Much of this issue in terms of resistance can be solved by adding more metal to the contact grid area. Though this is effective, there is still a trade off in terms of cost to coat the entire cell, as well as the ever-present coverage area vs. exposed semiconductor trade off. To solve this, scientists and engineers are

looking toward transparent conducting layers, such as indium tin oxide and newer 2D materials such as graphene.

Graphene Background

The discovery of graphene as by Geim and Norkvorst in 2004 and subsequent exploration of its properties caused an explosion of research and excitement around graphene and 2D materials. Graphene consists of a layer of carbon atoms arranged in a hexagon which displays incredible strength and durability properties. It has been shown that though a single atomic layer thin, graphene can function as an almost perfect barrier layer, with a strength that is greater than that of steel. The symmetric nature inherent to the bond structure of graphene make it a material which has a unique electronic dispersion relation in which the conduction and valence bands of graphene's electronic structure actually meet at the Brilliouin zone edge. The unusual shape of graphene's band structure allows for quantum states to exist at room temperature and cause graphene to possess outstanding transport properties. Graphene has theoretical mobility of over 200,000 $\frac{\boldsymbol{cm^2}}{\boldsymbol{V^*s}}$ and has exhibited ballistic transport on micron length scales.[15] This mobility can be utilized as very low resistance values for a small amount of material, and thus can help create a resistive layer used to lower series resistance in a photovoltaic device. Why does graphene have such amazing transport properties? A brief explanation of the physics behind graphene is necessary to gain an understanding of the phenomenon of graphene transport and how it can benefit photovoltaics.

Theoretical Graphene mobility

In examining graphene's theoretical mobility, it becomes readily apparent that the unique symmetric structure of graphene and its molecular thinness enable its transport characteristics. A standard graphene unit cell has two carbon atoms connected by a σ-bond, which in bulk graphene combine in specific unit vectors to create a hexagonal lattice of atoms with 3 σ-bonds from one carbon atom to its nearest neighbors. The fourth bond that exists for each carbon atom is a π-bond, which due to the single layer nature of graphene as well as the small atomic lattice spacing between carbon atoms, acts as a band. [16] This π-band exists out of plane of graphene, and as such is an excellent method to transport charge anywhere along the sheet of graphene. As seen in Figure 7, the π-band extends between all carbon atoms, and enables the ballistic transport of charge carriers across long distances. This band is very easy to interfere with as anything on the surface of graphene, or existing on the substrate upon which graphene is transferred, will negatively impact the transport of graphene. [12, 14]

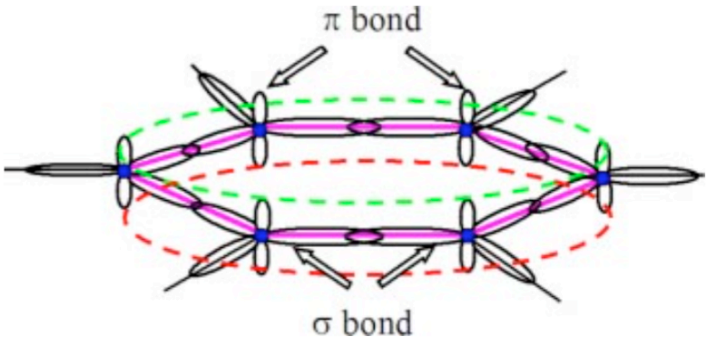

Figure 7: Band Structure of graphene [16]

This band structure of graphene is governed by the tight binding Hamiltonian model and is shown in regards to x and y by Fig. 8. It exists symmetrically across graphene until the K and K' points where the behavior of graphene as a transport medium

changes to a linear function with regards to k. This function shown in Equation 1 causes the quantum mechanical behavior exhibited at Dirac points, and is known as a Dirac cone.

$$E_{\pm}(k) \approx \pm \hbar v_f |k\text{-}K| \quad (1)$$

This Dirac cone equation is limited by the fermi velocity, which means that graphene has a conductivity that is limited by both temperature and substrate material. Though limited, this value is higher than most other known materials and in fact approaches the highest mobility's ever observed in nature. [18] This also implies that graphene exhibits 2D Dirac fermion behavior, and through the tight binding model graphene actually has a minimum conductivity; a characteristic not seen in many materials systems. [18]

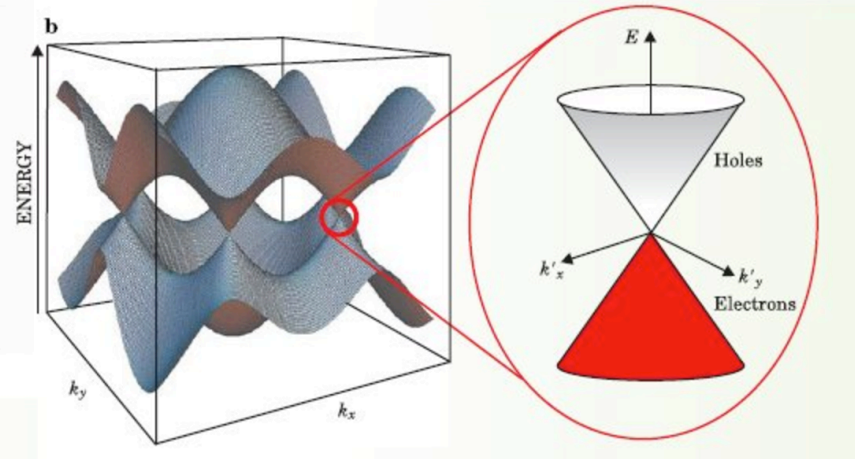

Figure 8: Electronic Band Structure of Graphene & Dirac Cone. The band structure of graphene is different from that of most other materials as it meets at the edge of the Brillouin zone. These leads to graphene displaying relativistic transport properties at room temperature. [15]

Phonon transport

Graphene attracts interest as a material as not only does it have abilities as a transporter of electrons, but also as a ballistic phonon conductor. The band structure of

graphene as a phonon conductor can be described by the Newtonian equation of equality of motion shown in Equation 2. *[15]*

$$-\sum_m \Phi_{m,n}\, \vec{u_n} = \omega^2 \vec{u_n} \quad (2)$$

Effectively, the two atoms in a unit cell of graphene are modeled as identical springs with three dimensions of freedom of motion. Each of these atoms is directly affected by the atoms it is bonded too, and indirectly effected by the atom's bonded to its nearest neighbors. The acoustic and optical bands of the graphene meet at the edges of the Brillouin zone and lead to mean free paths of graphene being as large as .775 μm. [19] This is coupled with graphene's large speed of sound, to make the thermal conductivity of graphene one of the theoretically highest possible values recorded for a material. [20] Having such a strong ability to conduct phonons can be useful in applications for cells like those of GaSb, as being exposed to TPV radiation carries with it a significant heat load.

Though these mobility values are theoretically high, graphene suffers from deviations in its ideal behavior due to contamination that can occur in both fabrication and transport of graphene. These are issue that scientists and engineers are looking to improve, so as to be able to capitalize on graphene's outstanding material properties.

Non Theoretical mobility

Graphene is limited from its theoretical limit because it is assumed that all graphene fabricated inherently has defects. The defects in graphene generally exist in two forms, and prevent it from exhibiting its theoretical functions.[12, 15] They exist as actual physical defects in a graphene monolayer, or trapped charges and defects on the substrate of a graphene material that induce defects on the graphene surface. [15] The

surface of graphene plays perhaps the biggest role in determining the variability of graphene, as the morphology of the substrate can alter carrier concentrations by as much as $2.3*10^{11}\frac{1}{cm^2}$ [21] The defects imparted onto graphene during the transfer process cause changes in doping levels as well as issues with long range order which negatively affect transport. [22]

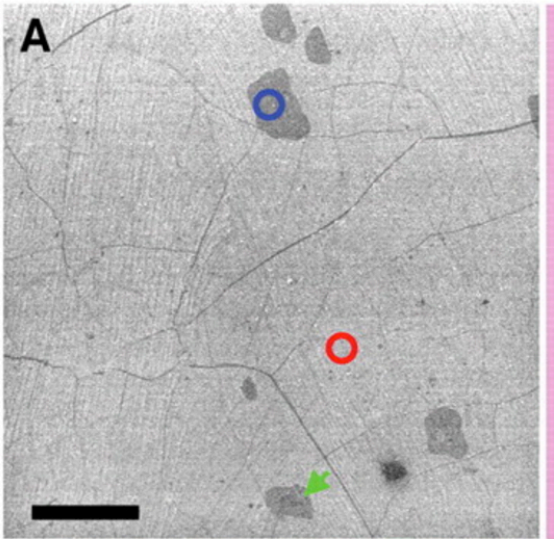

Figure 9: SEM image of CVD grown graphene with defects. The red circle represents pristine graphene grown. The blue and green cicrcles represent places where islands of double layer graphene were grown. Spots like this appear randomly during the growth, and can be deleterious to material properties and act as stress centers with cause cracks to occur, like those displayed in the image. [22]

Exfoliated graphene mobility

Exfoliated graphene was the first form of graphene fabricated and was the only kind of graphene that was capable of being created in the infancy of graphene research. As such there are many measurements and experiments involving exfoliated graphene which confirm its properties. Exfoliated graphene exists in flakes fabricated by the so called "scotch tape method", which consists of taking a sample of highly ordered pyrolytic graphite and using scotch tape to gradually reduce it in thickness until a few single layer flakes remain.[23] These flakes have been documented in a variety of size

ranges, but are limited to a maximum area of a few millimeters. Beyond this, the flakes start to become unstable and will generally break and crack during the transfer process. [15]

For the pieces that can be transferred, mobility's have been exhibited in the range from as low as 10,000 to as high as 200,000 cm^2/V-s.[15] Variability in regards to this mobility is due in part to the transfer method, but also is greatly impacted by the substrate upon which the graphene is transferred. The method for assessing these mobility measurements is using a gated Hall bar to both measure the mobility of a substrate, as well as assess its behavior under both positive and negative voltage. It was observed from these measurements that graphene possesses ambipolar transport behavior and is symmetric in its conductivity, confirming the Dirac cone as its band structure.[15] Observing figure 10 compared to figure 11, it is easy to note that the minimum point of conductivity for the exfoliated graphene is significantly offset from that of the theoretical one. This shift is caused by p-type dopants which cause a shift in the band structure of graph. [15] Graphene transferred onto Silicon typically demonstrates a lower mobility from graphene suspended on a substrate as there is less inference in graphene's band structure.

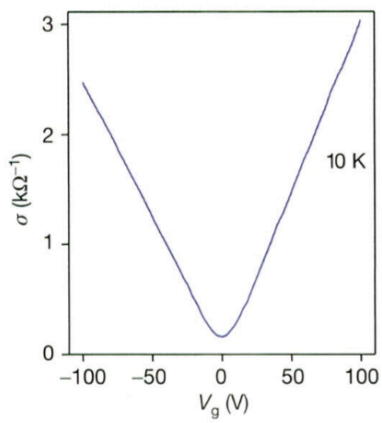

Figure 10: Theoretical response of Graphene under an electric field. This is what would be the expected response of transferred graphene. [15]

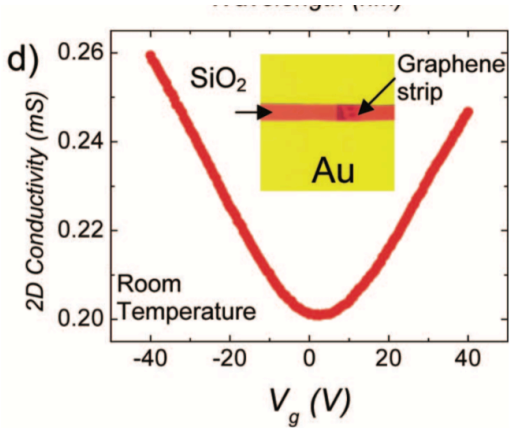

Figure 11: This is the experimental electrical response of transferred graphene. It is expected that this response would not be ideal because the measurements of the transferred graphene takes place at room temperature(~273°K) compared to the theoretical calculations done at 10°. [24]

The thermal conductivity of graphene for exfoliated graphene has been measured using suspended graphene with a non-contact laser method. [19] This is the most common method for measuring graphene thermal conductivity, as suspended graphene prevents any interaction in phonon transport with the substrate. [24] The thermal conductivity of graphene via exfoliation was measured using a suspended Raman sample and was shown to be around 5300 W/m-K. [19] An interesting aspect of these thermal conductivities is that they can in fact be altered by the medium in which the measurements are taken, where the thermal conductivity can vary by as much as 1,000

w/mK depending on whether the sample is under vacuum, or in a gaseous environment. [24] The thermal conductivity of exfoliated suspended graphene on a whole is some of the highest seen in science, with the thermal conductivity of graphene being five orders of magnitude higher than that of air. [25]

CVD Grown graphene

Graphene became a topic of greater interest in the electronic material's community after the discovery of the ability to grow graphene using chemical vapor deposition. Graphene could thus be grown to flakes of sizes larger than a few millimeters on a metal substrate and transferred, using a repeatable process.[26] This enlivened the scientific and industrial community as large scale growth of single layer graphene enables the possibility of graphene integration with devices. This form of graphene has exhibited a large variety of transport values on different substrates and with different transfer methods. Each of these methods has been proven to be successful, with minor processing tweaks helping the mobility of graphene to improve marginally. The first graphene grown by CVD was transferred onto SiO_2 and had a tested mobility of between 200-2000 $\frac{cm^2}{V^*s}$. [26] This wide variability is due to one of the inherent drawbacks of CVD grown graphene; it has grain boundaries which negatively affect the growth of graphene. Later experiments have optimized this process and improved the mobility of CVD graphene, but the room temperature mobility of graphene produced via CVD has not equaled the mobility exhibited by exfoliated suspended graphene.[27], [28]

This problem is easier to observe in the phonon mobility behavior of CVD grown graphene, which until recently has had mobility's generally lower than that of exfoliated

graphene. The thermal conductivity of CVD graphene was shown to be as high 2500 $\frac{W}{m\text{-}K}$, and recent advances have shown that CVD grown graphene can have a mean free path as long as 28 μm. [29] [30] Though not as high as exfoliated graphene, CVD-grown graphene still possesses thermal transport characteristics significantly higher than most conventional materials.

Graphene & GaSb

GaSb photovoltaics are an immature technology that stand to improve considerably with development in terms of both fabrication and crystal growth. The characteristic resistance issues which effect GaSb are problems that must be addressed for the technology to be implemented industrially. Graphene presents a good opportunity to solve these issues, as well as investigate if the phonon conduction capabilities can improve PV performance. Combining these two technologies represents an opportunity for scientists and engineers to gain a greater understanding of both graphene and GaSb photovoltaics.

Chapter 2: Fabrication and Optimization of PV Devices

Fabrication:

GaSb-based PVs are divided primarily according to the manner in which the substrate material is produced and the technique used to introduce dopants into the device layers. Many of the cells currently produced for GaSb-based photovoltaics use a process known as metal-organic chemical vapor deposition (MOCVD) to grow the full structure of the PV, consisting of a lowly-doped base layer (frequently the semiconductor substrate) and a thin, heavily-doped emitter layer that is closest to illumination source. Doping of the emitter layer is commonly accomplished by either dopant surface diffusion, or during the actual growth of the crystal. The dopant diffusion leads to very high dopant density as much as the solid solubility limit, but often results in poor emitter quality as dopant diffusion can cause defects to form and lower minority carrier lifetime.[31] To mitigate these defects, some devices use molecular beam epitaxy (MBE) to grow the emitter layer (and subsequent emitter doping). Traditionally, solar cells utilize a p-type base to take advantage of the higher mobility of electrons compared to holes. However, it is much easier to grow high quality n-type GaSb substrates or wafers, and as such our device design uses a p-type emitter on an n-type base configuration.[32] This design has been proven to be successful in terms of improving the SRH recombination lifetime of electrons [33].

The devices grown for our group's purposes were developed to capitalize on the MBE's ability to grow low background defect material infused with large dopant concentrations This low defect density leads to a longer lifetime than other similarly

doped materials such as Zn or Te-diffused. [33], [34] As the minority carriers are the governing carrier in PV operation, it is beneficial to grow the best emitter layer possible to maximize both the number of carriers as well as their probability of getting to a location and being collected. The p-type emitter layer was grown to 670 nm via an MBE growth purchased from IntelliEpi and doped to 5e18 cm^{-3} [33], [35]. This emitter thickness has subsequently been determined to be too thick after examination of the structure via modeling [33]. The p-type emitter was grown directly on the Te-doped, n-type GaSb substrate which minimized the thickness of required epitaxy. [33]

Back Metal Contact

In order to collect the photo generated carriers in the PV, there must be some form of contact on the front and back of a photovoltaic to apply to voltage to. These front and back electrodes on the cell must be of a metal with low resistivity, and have a work function calibrated to act as an ohmic metal contact. The metal stack used during fabrication was Pd (87Å)/Ge(560Å)/Au(233Å)/Pt(476Å)/Au(2000Å) as it has been proven to give ohmic behavior to n-type GaSb and is an improved barrier to metals penetrating into the semiconductor substrate. The metal is deposited on the back contact using e-beam evaporation after a 1:3 HCL:H_20 etch for 30 seconds to strip off any residual oxide that exists on the GaSb Surface. This was followed by rapid thermal annealing at a ramp rate described in the appendix. The back contact of the photovoltaic covers the entire back side of the device, as no light needs to penetrate through the surface. This is helpful in device design as the resistance of the back contact as shown in Equation 3 is directly proportional to the width of the device; having a wide device

counteracts the length of the device and enables the thickness to be the only determinant of back contact resistance. [36]

$$R = \frac{{}^{*}L}{t^{*}W} \qquad (3)$$

Front Metal Deposition

The front contact was formed via the liftoff technique and used a e-beam deposited Ti/Pt/Au (500/500/3000 Å) metallization. First AZ 5214 EIR photoresist was spun onto the wafer at 2500 rpm for 60 sec to get an estimated height of 1.5 μm and subsequently exposed by a Karl Suss MA6 mask aligner system with light of wavelength (405 nm) for approximately 2 seconds. This was then immediately followed by a bake on a hot plate at 120 C for 60 seconds. The photoresist was then subjected to a flood exposure for 30 seconds to allow for image reversal, and subsequently developed. The step height of the photoresist as well as feature size of the patterns was measured by a DekTak surface profilometry system.

For some of the GaSb PVs, it was decided that to facilitate later packaging of the cells by wire bonding, an additional layer of metal needed to be deposited. This was done by following the same patterning process as the first metallization step, but with an additional sequence of Ti/Au (500/2000 Å). This was enough metal to allow for effective packaging of the cells to allow for future full TPV measurements.

The cell substrates were then patterned again and subjected to a mesa etch solution of HCL:H_2O_2:H_2O (50:1:150) for 15 minutes at 15C. [32] The cells were then diced using an MA-100 dicing saw to enable easier testing.

Shading Loss Prevention

In a solar cell, the collection mechanism (and inherently the cells efficiency) for capturing photo-generated carriers is tied in part to how much of the front (illumination facing) side of the photovoltaic is covered by metal versus the quantity of the device exposed to electromagnetic energy. This inherently creates a tradeoff in terms of capturing photo-generated carriers with metal contacts versus exposing photoactive areas of the device to light which actually creates the carriers. The schematic of PV operation in Figure 12 shows how shading loss occurs in a photovoltaic with an opaque front metal contact. Having less coverage area also changes the series resistance of the cell, as resistive networks like the crosshair or fishbone metal patterns of a solar cell have vastly different resistances compared to simple large coatings of a material such as indium tin oxide or graphene.

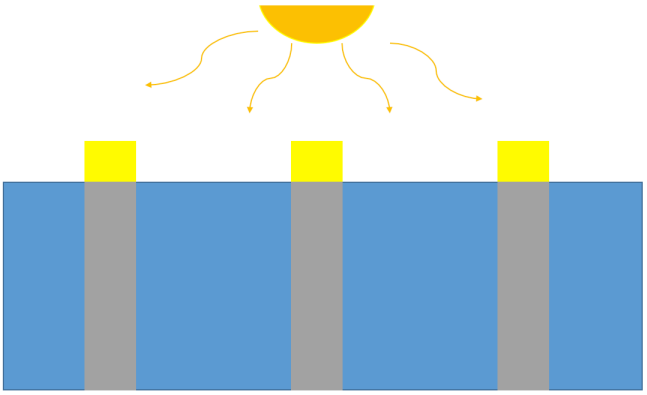

Figure 12: Solar Cell with Shading Effects

The tradeoff between the coverage area and the resistance of the metallization is a challenge in the GaSb materials system. It is the clichéd "Catch-22" of Joseph Heller; we need more metal coverage to collect photo-generated carriers, but more coverage area

means less photo-generated carriers. As scientists and engineers we can use the tools of optimization and computer simulation to solve these problems.

To solve the front contact pattern issue, first the physical production of the solar cells was considered. It is known that in the processing of metal contacts, it can be difficult to create certain features that have curves or non-orthogonal patterns as liftoff of deposited metals can fail. To that end, the front contact pattern of the devices designed at Virginia Tech was constrained to a single bus bar with hatched finger design as shown in Figure 13. This enabled for easy determination of a resistor network because the fingers and bus bar would have consistent lengths and widths. In analyzing this resistor network, the sheet resistance of the p-type emitter layer between each finger had to be factored into the optimization algorithm in order to simulate the lateral spreading of current in the semiconductor. This is a function of dopant concentration and was considered fixed for the purposes of algorithm development at a value of 100 ohms/square. The resistivity of each metal finger was fixed and considered to be constant as well. To engage in an optimization of the cell, the coverage area of front metal was fixed at 10%.

The resulting network is exhibited in Figure 14 and was solved using a computer program written in Matlab. The network was solved in a sequence of steps where in a front contact design like that shown in Figure 13 can interpreted as the resistive network in Figure 14.

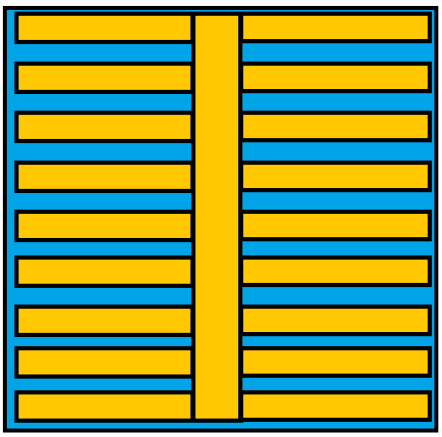

Figure 13: Sample image of a solar cell front contact area.

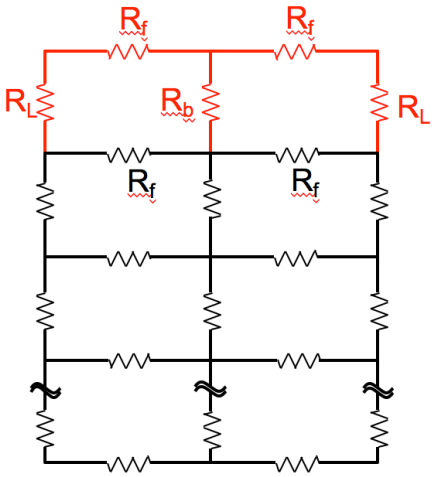

Figure 14: A resistive network that is representative of the standard front metal contact exhibited in Figure 13.

Using the following methodology, the cell was reduced to a single resistor network. The first step consisted of consolidating resistors in series (the R_f and R_L values) into one value for each branch, indicated as R_1 and R_2 in the figure, with the R_B relative position changed for visualization purposes.

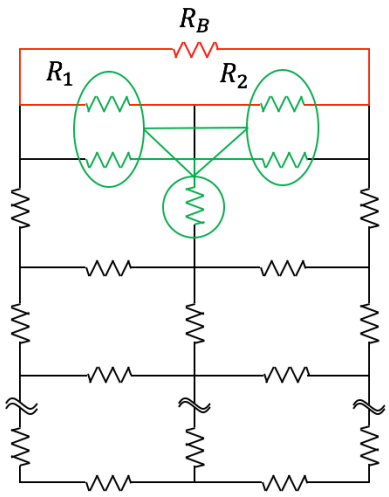

Figure 15: Consolidation of parallel resistors. This is the first step in the optimization process and is both the first and last step of the process. By doing the consolidation in this way solving the rest of the network is an easier process.

This positioning was then further consolidated by adding together the two parallel resistors indicated in Figure 15 by green circles, which allows for a reformation of the network into that depicted by Figure 16. At this point, Figure 16 can be further reduced by consolidating the indicated parallel resistors, and reconfiguring the two Δ arrangements indicated by black circled resistors to arrive at a configuration that is indicated by Figure 17. The resistor network in Figure 16 can be reduced by adding the resistors at the top of the network in series, and then changing the middle Y arrangement of resistors to a Δ configuration. This arrangement (Figures 16 & 17) form a cycle where resistor arrangements can be cycled from Δ to Y and Y back to Δ, consolidating parallel and series resistors when available, which enables the designs of each resistor network to be assessed.

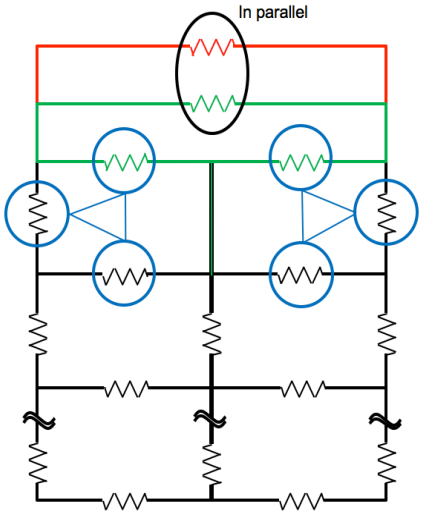

Figure 16: Part A of the resistive network consolidation process. By following this process, the typical resistive network that is most fabricated photovoltaics devices can be reduced to a manageable value and compared to other networks. Varying the value of each resistor through aspects of the device design such as finger or bus bar width, can give valuable insight as to the limiting series resistance characteristic of a device design.

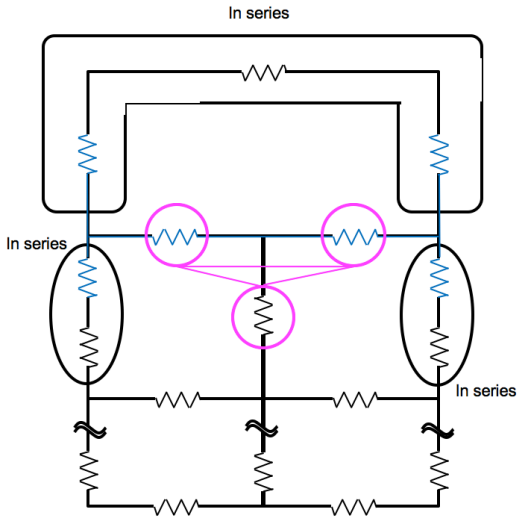

Figure 17: Part B of the resistive network reduction sequence. By following this process, the typical resistive network that is most fabricated photovoltaics devices can be reduced to a manageable value and compared to other networks. Varying the value of each resistor through aspects of the device design such as finger or bus bar width, can give valuable insight as to the limiting series resistance characteristic of a device design.

This algorithm enabled rapid calculation of resistance values for each cell configuration, as well as the incorporation of shading resistance. When designing the algorithm, the minimum value of finger size was taken to be 10 μm, and the minimum

bus bar width was taken as 100 μm as it would be difficult to ensure consistent photolithography and metal liftoff with features smaller than this on equipment available in the Micron Technology Semiconductor Processing Laboratory cleanroom. When analyzing the results, it became apparent that there were three different decision criteria for creating the optimal solar cell contact configuration. The width of the bus bar, finger width, and number of fingers while staying at 10% coverage are the ways in which the resistance of the cell were be modified and optimized.

Though it is possible to create optimization points in the algorithm, it is difficult to visualize this information with 2D Charts. An attempt to give a better understanding of optimization points in the algorithm is shown in 18. Figure 18 is a visualization of how changing bus bar width modifies the overall front metal resistance (which includes the semiconductor sheet resistance) of the device design. Note the finger width must be fixed for each iteration of bus bar width and finger number. They are not capable of being visualized concurrently in a 2D graph (though it is factored into the algorithm). For finger widths considered, the bus bar width is most effective in the 300-375 μm range. The rationale behind this can be more easily understood by observing Figure 18, where the finger number is varied with set finger widths. The minimum of these values, which is around 0.6 Ω, corresponds to the relative minimum that exists in across each of the 2D plots. There is a general trend in which having less fingers that are wider has lower overall resistance, but this trend is inexact, and later optimizations of the algorithm code revealed that the resistive loss of p-type emitter layer between fingers was underestimated. Critically looking at the optimization trade off, it becomes apparent that

there is no exact “best” cell design, and as such it made sense to try different cell designs with varying finger numbers, widths, and bus bar widths.

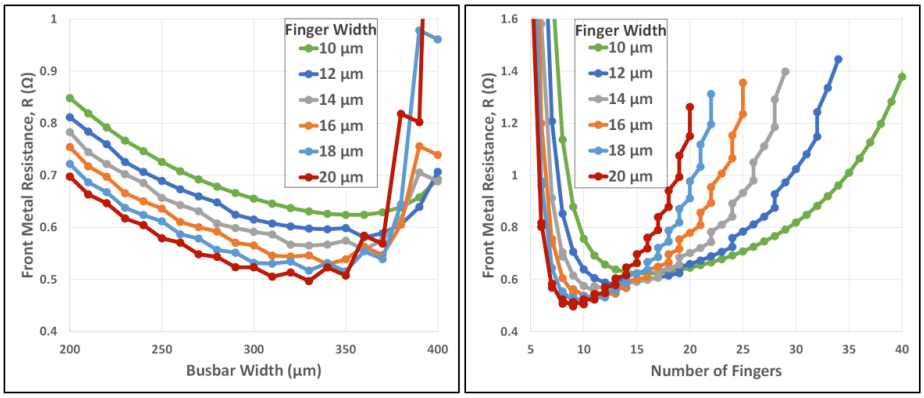

Figure 18: : 2D representations of resistive network consolidation. The figure on the left varies the busbar width and finger width with a number of fingers that fulfills the 10% coverage area requirement. The figure on the right varies the number of fingers and finger width with the busbar width being changed to compensate for the 10% coverage area requirement. The minimum resistance values for each finger width correspond between figures.

Optimized Cell Designs

Three optimized front contact designs were selected, and incorporated into a photolithography mask with three other designs that existed previously (with some necessary packaging modifications). The three designs chosen by the optimization program are cells 2, 5, and 6 shown in figure 19, renamed as alpha, beta and gamma. Cell designs Alpha and Beta are similar in terms of finger number but differ in regards to bus bar width, which was a conscious attempt to see if there was a noticeable difference from having a wider bus bar with wider finger spacing’s. The Gamma cell is vastly different from the others in the optimization, and was chosen before it was discovered that the optimization program contained the error which did not account for the actual power loss that would occur from having fewer fingers. It also under-estimated the sheet resistance between these fingers and resulted in a design which did not exhibit the resistance characteristics expected. Cell 1 was an old design featured in several publications that

was used as a control to compare our optimized designs.[32], [35] Cells 3 and 4 were designs obtained from collaborators in the MIT Joannopoulos group, with cell 4 being modified to have a larger bus bar to aid in wire bonding. The designs were printed onto a quartz mask and a second version of the design with all of the features 1-2 μm smaller was created for second metallization step that improves the ease of wire bonding.

Cell	Bus Bar Width (μm)	# of Fingers	Finger Gap (μm)	Finger width (μm)	Coverage Area (%)
1 - Control	300	20	228	25	15.2
2 - α	320	19	269	10	9.87
3 - Mod MIT	250	50	90	12	16.2
4 - MIT	156	50	90	12	14.44
5 - β	250	26	192	10	9.78
6 - γ	270	6	942	40	9.80

Table 1: Cell design parameters selected for the photomask. Cell's 2, 5, & 6 were designed at through the optimization program. Cell's 1, 3, & 4 were from previous publications and collaborators

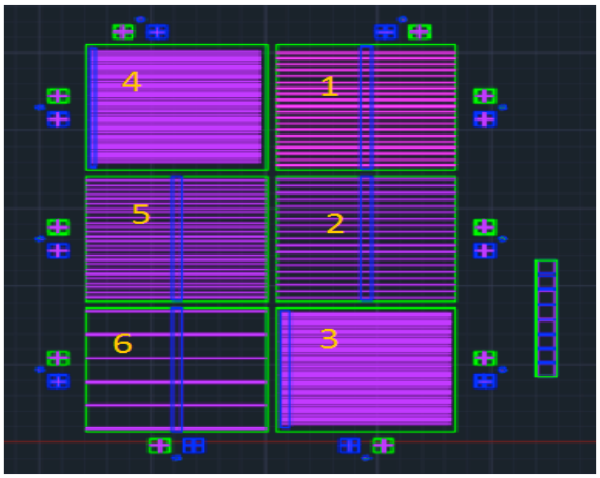

Figure 19: Cell Designs drawn in AutoCAD. These 5 x5 mm cell designs were repeated across the entire 4 inch by 4 inch mask area to make production easier.

Cell Characteristics

After the cells were fabricated, they were tested under AM1.5 conditions using an Oriel QE solar simulator. These tests were used to assess the quality of both the fabrication process as well as the effectiveness of the program in reducing the front metal contact resistance of the devices. For each respective device type, the average of the shunt resistance, short circuit current density, and series resistance were all presented as they give a more complete picture of the current generation techniques of a typical device. It is prudent to note that the short circuit current density has been shown both compensated and uncompensated for the shading of coverage area. This gives a better indication of the real PV behavior.

Cell #	Avg. Efficiency (%)	Avg. R_S (Ω)	Avg. R_P (Ω)	Avg. J_{SC} (mA/cm^2)	Avg. V_{OC} (V)	Coverage Area (%)	Avg. J_{SC} (mA/cm^2) Cov.

							Comp.
1 - Control	2.57	13.17	93.04	29.2	.205	15.2	34.40
2 - α	2.16	16.03	83.05	28.16	.202	9.87	31.24
3 – Mod MIT	1.65	17.88	97.11	22.84	.194	16.2	27.27
4 - MIT	2.97	10.84	343.87	31.34	.204	14.4	36.61
5 - β	2.36	15.46	151.22	27.98	.195	9.78	31.01
6 -ϒ	1.34	22.92	68.50	23.28	.192	9.8	23.27

Table 2: Average GaSb single metallization cell characteristics under AM 1.5 conditions. The J_{SC} difference between the control and VT designed cells is marginal and as such it can be said that the optimization program was effective. The poor J_{SC} characteristics of cell 6 show the inherent problem with designs that have few fingers; the emitter is still too resistive to have comparable conduction compared to smaller open semiconductor surfaces with more fingers.

The average J_{SC} values exhibited are comparable GaSb-based PVs under AM1.5 conditions that are reported in the literature. [34] The highest J_{SC} for several of these cells was over 40 mA/cm^2 (when compensated for coverage) and it is in a realm that is higher than most other fabricated GaSb PVs. (see appendix B of full results)

Comparing the series resistance values between cell designs, the cells with less coverage area have more series resistance. This is to be expected because as was implied by Equation 3, less metallization has a higher series resistance, and the sheet resistance also becomes a factor in a more open finger design. Because of the presence of a significant series resistance in some of these designs, the J_{sc} is not only affected by the areal coverage of the metal fingers, but also the series resistance and the shunt resistances

(see Chapter 3 equations). Comparing designs 2, 5 and 6, which have the same finger coverage, the deteriorated J_{sc} of design 6 is due to the significantly higher series resistance.

In contrast, for a group of GaAs PVs that was also processed with the same device layouts, this J_{sc} difference between designs 2, 5 and 6 was not observed because of a much higher shunt resistance that acts to mitigate the deleterious effect of the series resistance on the J_{sc}. The measured V_{OC} values are lower than those reported in the literature (typically 0.3 volts) with comparable J_{SC} values. [37] The explanation for this behavior is also explored in the next chapter.

Cell #	Efficiency (%)	R_S (Ω)	R_P (Ω)	J_{SC} (mA/cm^2)	V_{OC} (V)	Coverage Area (%)	J_{SC} Cov. Comp. (mA/cm^2)
1 - Control	4.95	4.09	638.57	41.52	.211	15.2	49.96
2 - α	4.43	4.51	252.27	37.77	.210	9.87	41.91
3 – Mod MIT	3.55	5.23	193.77	30.91	.203	16.2	36.86
4 - MIT	4.43	4.23	531.15	37.17	.210	14.4	43.43
5 - β	4.08	4.39	1109.88	34.42	.208	9.78	38.15
6 -Υ	2.33	10.1	88.25	30.24	.200	9.80	33.53

Table 3: Results from a double metallization a single process run of GaSb substrate. These results are not an average, and are a good indicator of the second metallization process improving overall fabrication of the photovoltaic devices. The addition of the metallization layer caused the series resistance of most of the devices to go down to a consistent level (around 4 Ω). The exception to this is cell 6, where the resistance drops to only 10 Ω. This exemplifies the resistance that exists due to large exposed emitter layers of the semiconductor.

2nd metallization

Originally, the a 2nd front-side metallization was designed to enable easier wire bonding, as thick layers of metal were necessary to wire-bond cells with the equipment immediately available. After examining the testing data, it became apparent that after adding the second metal layer, these devices exhibited improved series resistance. For most designs, the values are consistently around 4-5 Ω, which is limited primarily by the p-type emitter sheet resistance. In contrast, the series resistance value exhibited by 6-ϒ is about 10 ohms. The failure of the J_{SC} of cell 6-ϒ to not grow by as much as the other VT designed cells (2 & 5) and this difference is an excellent indicator of how designs with a larger finger separation can have series resistance limited by the emitter sheet resistance. Graphene can overcome this sheet resistance problem as will be shown in Chapter 3.

By significantly improving the R_S in designs 1-5, the second metallization had a positive impact on J_{SC} as the value improved for these fabricated devices. Simultaneously, the shunt resistance increased in these devices, which is not expected for cells that merely have additional metal thickness in the fingers. How is this result explained? The presence of the shunt defects in the MBE-grown GaSb emitter layer is a known problem in this material system. The lower resistance metal fingers created by the 2nd metallization more effectively bypasses the shunt defects in the epitaxial material. This is why an increased shunt resistance is observed in the 2nd metal versions of the GaSb cells.

It is puzzling that substantial improvements made to the shunt resistance did not give comparable improvements to the V_{OC} measurements. Any V_{OC} improvement should be marginal at best as the formula to calculate implicit V_{OC} from solar cell data is

exponential, but the fact that it remained at the same level even with a substantial improvement to all other solar cell performance characteristics speaks to a larger scale problem in this devices fabrication. The difference in results between single and double metallization inspired the work with graphene and deeper analysis into device operation that became the basis of the following chapter in this work.

Chapter 3. GaSb Parameter Extraction & Graphene Analysis

Diode Equation Basics

When examining the data in terms of how the GaSb cells function, it is easy to underestimate the impact of series and shunt resistance on how photovoltaic devices operate. Looking at the data received from the solar simulator, it would be incorrect to assume that we are observing the ideal performance of the cell since parasitic resistances can be an issue in relatively immature materials technologies such as GaSb. At $V=V_{OC}$ (I=0) the dominant resistance value exhibited by the cell is the series resistance, which is in series with the much lower diode resistance. Conversely, at $I=I_{SC}$ the observed resistance is commonly due to the shunt resistor, since the diode resistance is typically much higher and the series resistor relatively insignificant at this operating point. In most PV cells like those of silicon or GaAs, this is the case. However, given the relatively low values of R_P and high values of R_S exhibited in our GaSb cells, we cannot safely make these simplifying assumptions. The ideal performance of the GaSb cells is actually considerably masked by the parasitics. The following discussion shows how the ideal parameters can be extracted.

First we must establish a fundamental equation for solar cell operation. For a solar cell operating under forward bias, the characteristic equation is displayed in Equation 4 below (assuming operation in the 1st quadrant):

$$I = I_{PH} - I_0 \left[\exp\left(\frac{V+IR_s}{nV_{th}}\right) - 1\right] - \left(\frac{V+IR_s}{R_p}\right) \qquad \textit{Equation 4}$$

where I is the current exhibited by the device, V the voltage applied to the device, I_{PH} is the photocurrent generated in the device, I_0 is the reverse saturation current flowing through the PN junction, R_S is the series resistance exhibited by the device from its front and back metal contacts (as explained in chapter 2), R_p is the shunt resistance of the device, V_{th} is the thermal voltage of the device at a temperature of 300 K, and *n* is the ideality factor for the devices (n = 1.1). [33] This equation represents the single diode model, which has been chosen for these devices as it is effective enough for comparative analysis of the fabricated cells. It is useful to gain information about how the device operates by analyzing the cell at its axis crossings on the IV plot. At $V=V_{OC}$ there is no output current flowing out of the device and as such, it is possible to reduce Equation 4 to Equation 5 shown below.

$$I_{ph} = I_0 \left[\exp\left(\frac{V_{OC}}{nV_{th}}\right) - 1\right] + \left(\frac{V_{OC}}{R_P}\right) \qquad \textit{Equation 5}$$

In examining the way in which the cell behaves at I_{SC}, another reduction in the parameters relating to the behavior of the cell can be made. This expression is shown in Equation 6 below.

$$I_{SC} = I_{PH} - I_0 \left[\exp\left(\frac{I_{SC}R_S}{nV_{th}}\right) - 1\right] - \left(\frac{I_{SC}R_S}{R_p}\right) \qquad \textit{Equation 6}$$

This gives a set of two equations with four unknowns; in most photovoltaic devices two of those unknowns (the series and shunt resistance) can be independently extracted from the IV characteristics.

Circuit analysis

In its simplest form, a PV consists of a current generating source, a diode in series with a resistor that represents the front contact resistance and spreading resistance of the cell, as well as a shunt resistor in parallel with the diode. The series and shunt resistors

are constant, but the diode is variable and is found from the derivative of the diode equation with respect to voltage, which is shown in equations 3 and 4:

$$R_{diode} = \frac{dV}{dI} = \frac{nV_{th}}{I_{Diode}} \qquad \textit{Equation 7}$$

This allows for the simplification of Equation 4, which is a transcendental equation that is solvable if assumptions are made about the relative sizes of the resistors at the V=0,Voc operating points. In doing this, we can say that the measured R@V_{OC} is reduced by the diode resistance to find the R_s, where it is assumed that $R_P >> R_{Diode}$ at V=Voc. (full derivation in the appendix C)

$$R_S = R@V_{OC} - \frac{V_{th}{}^{*}n}{I_{ph}} \qquad \textit{Equation 8}$$

Conversely we assume that $R_{Diode} >> R_P$ at V=0, and therefore the shunt resistance can be found from the following:

$$R_P = R@I_{SC} - R_S \qquad \textit{Equation 9}$$

Figure 20 can help visualize these last two assumptions about the relative sizes of R_{Diode} and Rs at the voltage limits of the operation of the cell.

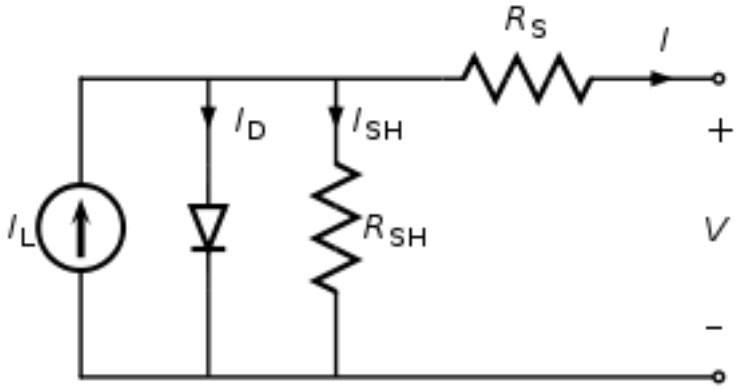

Figure 20: Solar Cell Circuit Diagram. The diode resistance (R_{Diode}) changes greatly under the V_{OC} and I_{SC} conditions. Analyzing the circuit diagram at these conditions and making assumptions about the resistance of the diode helps to be able to calculate the exact R_S and R_P values for the GaSb devices. Knowing these

parameters allows for calculation of I_0 and I_{PH}, which give insight into why the GaSb PV's do not perform as expected. [14]

For the GaSb devices fabricated, there is a broad variation of the parasitic resistance values, and their behavior is interesting enough that it bears comment. In these devices the dV/dI slope at V=0 is not equal to Rp and the dV/dI slope at V=Voc is not equal to Rs as is the generally the case in mature photovoltaic material systems that have the desirable characteristics of a very low series resistance and very high shunt resistance. For GaSb PV technology, however, the correction factors introduced in Equations 8 and 9 are absolutely necessary.

Examining the data in Table 4, the change between $R@V_{OC}$ to R_{Series} is obvious as the resistance decreases in all cases. The change between $R@I_{SC}$ and the R_P is greater in magnitude for most of the devices compared to the change between $R@V_{OC}$ and R_{Series}. The benefit of using equations 8 & 9 to remove these parasitics is apparent when the difference between J_{SC} and J_{PH} (both uncompensated for coverage) is examined. The J_{PH} (which is derived in the next section) is over 6 mA/cm^2 for all of the cells examined. This difference is significant enough that it justifies the extraction R_{Series} and R_P using equations 8 & 9.

Cell Name	$R@V_{OC}$ (Ω)	R_{Series} (Ω)	$R@I_{SC}$ (Ω)	R_P(Ω)	J_{SC} (mA/cm^2)	I_0 (A)	J_{Ph} (mA/cm^2)
Cell A	4.48	1.24	610.3	609.1	35.14	6.69E-6	41.14
Cell C	21.3	16.4	84.3	68.0	21.47	3.23E-6	29.70
Cell D	10.7	7.43	81.8	74.3	34.84	5.47E-6	42.74

Table 4: Measured PV parameters compared with their extracted values. The series and shunt resistances change after extraction, and when these parasitics are factored out of the cell characteristics to find the J_{PH}, the value of the parameter extraction is apparent.

I_0 and I_{Ph} Extraction

The system of equations set forth in Equations 5 and 6 are then used with the values of R_S and R_p calculated from measured data using Equations 7 and 8. This gives us 2 equations with the 2 unknowns of I_0 and I_{ph} , given that we assume an ideality factor, *n*, of 1.1 from previous results.[33] Solving this system of equations yields the following:

$$I_0 = \left[\exp^{-1}\left(\frac{V_{OC}}{V_{th}{}^{*}n}\right) * \exp\left(\frac{I_{SC}{}^{*}R_S}{V_{th}{}^{*}n}\right)\right]^{-1} * \left[I_{SC} * \left(1 + \frac{R_S}{R_P}\right) - \left(\frac{V_{OC}}{R_P}\right)\right] \qquad \textit{Equation 10}$$

$$I_{ph} = I_0\left[\exp\left(\frac{V_{OC}}{nV_{th}}\right) - 1\right] + \frac{V_{OC}}{R_P} \qquad \textit{Equation 11}$$

From these equations it is possible to analyze the intrinsic behavior of the cells without the influence of the devices' poor characteristic resistances.

Photocurrent Normalization

To characterize and understand the cells further, it makes sense to change the photocurrent to a value that is independent of factors that vary between cells. To do this the cell area (0.25 cm^2) as well as the coverage area (which is cell dependent) must be removed from the photocurrent characteristics of the cell. Each value was changed from to mA for normalization purposes. The results of each parameter extraction in terms of current were normalized and passed through equations 12 & 13.

$$J_{ph} = \frac{I_{ph}}{1000 * (.25\ cm^2)} \qquad \textit{Equation 12}$$

$$J_{ph\ Cov.Comp.} = \frac{J_{ph}}{(1 - Metal\ Coverage)} \qquad \textit{Equation 13}$$

Comments on the Intrinsic Jph Results

J_{SC} for most PV devices, like those of Silicon and GaAs, is a quantity which should be unaffected by the series and shunt resistances as the magnitude of each is such that according to equation 6, any variation in them will be of minor consequence. Looking at the change that is exhibited between J_{SC} and J_{PH} once the parasitic's are extracted gives validation to the parameter extraction process. The photocurrent change for each cell in Table 4 is at least 6 mA/cm^2, a change similar in magnitude to removing coverage compensation of fabricated devices (like that seen in chapter 2). Parasitic resistances in GaSb PV devices are detrimental to device characteristics, and the deleterious nature of these defects make the GaSb devices appear worse than their true behavior indicates. This shows that the current generation capabilities of the GaSb growth was excellent, but at some point in the fabrication process the shunt resistance was compromised, and the cells performance suffered. The application of graphene seeks to resolve some of these issues.

2D Material Solution to the Series Resistance

With the knowledge that the fabricated GaSb cells had relatively large series resistances due to the p-type emitter sheet resistance, ways to compensate for this situation were explored. Although the effect of series resistance on the short circuit current was mitigated with the introduction of the second metallization, the deleterious impact of R_s on the fill factor was still present. A lower sheet resistance was still required without having to increase the emitter thickness or doping concentration further, which would have decreased I_{ph}. Whatever additional conductive layer is introduced, it would

need to be mostly transparent to the wavelengths where GaSb PVs operate. This is where new technologies like 2D materials step in to fill the gap that the conventional processing technologies cannot provide.

By utilizing graphene's outstanding conductive properties as well as its nearly constant low percent optical transparency [15], [38], graphene stands to the improve sheet resistance of emitter layer through a surface application. Given graphene's impressive phonon transport properties, it is probable that the heat load that a single cell has to handle could be offset by the application of graphene layer. [15] Furthermore, graphene could potentially act as a surface passivation layer that would improve excited carrier collection, as well as act as a transparent conducting electrode. Graphene is a solution to the series resistance issue that is relatively low cost, and poses only minor processing issues with the potential for substantial device performance benefits.

Graphene Transfer Process

Since the discovery of the ability to grow single layer graphene (SLG) via Chemical Vapor Deposition (CVD) [39], the ease with which graphene can be used in technology has improved considerably. The process used for transferring these layers follows a standard method first reported in works by Reina et al. [39], but with minor modifications on several of the transfers. The graphene was purchased from University Wafer in 10 x 10 mm squares of copper film. Previously, a larger circle of graphene 4 inches in diameter was purchased from University Wafer, but it was found that cutting such a large piece of graphene damaged it before the transfer process could occur.

Each of the copper squares was cut into four 5x5 mm pieces by being held between two pairs of tweezers under tension and cut to prevent any wrinkling the foil itself. These cut pieces were then matched to each cell and made to be slightly larger to aid in the transfer process. Two methods were used for spin coating the graphene, with both benefits and challenges for each. Both methods utilized spun-coated 1.5 wt % PMMA diluted in anisole. The photoresist was spun at 500 rpm for 70 seconds to ensure a thick layer (over 1 μm) which made transfer easier. The samples were then baked at 80 °C for 5 minutes before being subjected to the standard etch and water bath procedure [39]. The methods diverged when it came to deciding how to mount the graphene samples onto the spinner in order to get them coated evenly by photoresist.

Transfer Method A

Method A consisted of taking a 10 x10 mm piece of graphene and directly put it onto the spinner, then depositing photoresist onto it. This method then required the copper sheet be cut into pieces large enough to cover the cells. Though this method garnered adequate coverage of the cell by photoresist, the spinner suction caused a small rip to form in the copper foil, in the shape of the suction head. This caused stress to accumulate on the foil, and would lead to graphene sheets breaking apart in the transfer process. It was also easy to observe that there were defects on the graphene surface that appeared during the transfer and caused the foil to break up and be lost. This process was used on most of the cells transferred, because although the process yield was low, it was still the most efficient way to ensure complete coverage.

Transfer Method B:

Though similar to method A, method B displayed an ability to transfer larger areas of graphene more effectively. The larger graphene sheets (10 x 10 mm) were first flattened between two glass microscope slides to remove any creases present in the foil. Though it could be said that this process imposes defects on the graphene, it is beneficial to take any ripples or bends out of the surface as it makes floating the graphene easier. A separate glass slide was then taken, cleaned, and dried thoroughly, after which a small water droplet was placed on the center of the slide. The graphene on copper foil was then placed over this droplet and a second slide was used to press the slide down into place, to create a good seal. The cell was then spun-coated on the slide to attempt to ensure that none of the defects that were instantiated from the vacuum tip would happen on these foils. These copper foil pieces were then cut into 5 x 5 mm squares in an attempt to match them to cells. This method resulted in very high quality graphene, but did not have a high yield rate as several times the deposited photoresist migrated to the backside of the graphene and made it impossible to complete a successful graphene transfer. These transfers did not result in good cell data, but when used for transferring complete 10 x 10 mm sections of graphene, the quality and ease of the transfer was better.

Graphene on TPV

After graphene deposition, the PV cells were tested under AM1.5 conditions in the same solar simulator as the initial measurements for each device. The cells were contacted on the metal pads as was done in previous measurements (not directly on graphene). It was assumed that even if contact was made through the graphene to the metal pad, there would be no issues with getting good results as graphene is conductive

enough to give consistent results. The goal of this analysis was to validate graphene as a way to reduce the series resistance in single-metallized GaSb devices, as well as assess whether the application of graphene had any surface passivation effects. The cells that were selected had J_{SC} values within the range exhibited by single metal devices, but all of which possessed relatively high parasitics.

Cell ID	Design #	V_{OC} (V)	J_{SC} (mA/cm^2)	R_{Series} (Ω)	R_P (Ω)	J_{PH} (mA/cm^2)	I_0 (A)
D	2	.182	17.73	23.37	67.73	24.38	4.71E-6
D + SLG	2	.180	19.56	18.89	74.51	24.97	5.84E-6
E	2	.195	26.36	16.96	50.91	35.85	4.53E-6
E + SLG	2	.196	28.03	14.7	52.27	36.43	4.64E-6
G	6	.200	32.24	14.28	31.01	47.72	3.78E-6
G + SLG	6	.203	39.65	7.58	44.04	46.68	4.7E-6

Table 5: Graphene on Single Metal TPV Device behavior. The graphene transfer reduces the parasitic resistance of the PV device and increases the J_{SC} of the cells. The V_{OC} and I_0 of each device remained the about the same and was within measurement error of testing.

V_{OC} & I_0 changes

The V_{OC} for the fabricated cells could not be expected to increase substantially after the graphene application, but for two out of the three cells the value went up. The I_0 stayed relatively the same across all transfers and judging it along with the other characteristics did not point to any of the changes in I_0 having a negative effect on the overall cell characteristics. The changes in both V_{OC} and I_0 were small enough that they could be considered as measurement error.

Characteristic Resistances

Though possible to be solved by the application of a thicker second metallization, graphene empirically presents a good path to reducing the series and increasing the shunt resistance of the GaSb fabricated devices. Looking at the change in series resistance from one device to the next, it is apparent that SLG reduced the series resistance for each device. For cells patterned with more fingers like cell D & E (cell design 2), the decrease in series resistance is less pronounced than cell G which has a relatively fewer fingers and large gaps between them. The series resistance in this cell is in fact halved, and experiences a sizable 13 Ω increase in the shunt resistance. This is the greatest increase seen between cells, and is more representative of how this application of graphene could impact these GaSb solar cells. The graphene seems to be more effective with sparse coverage areas as it can allow for favorable conduction paths between fingers, instead of through the bulk GaSb.

The graphene did not result in the same limiting series resistance behavior as was seen in the double metallization cells. The inexact nature of graphene transfer, as well as the lack of full coverage on most of the cells, is most likely the reason that this did not occur. The transport properties of graphene are beneficial to the GaSb PVs, and the changes in series resistances show the graphene transfer was effective in reducing parasitic resistances. Graphene is an acceptable solution to the series resistance problem that is worth transferring onto GaSb PVs.

Effect of graphene coating on J_{SC} & J_{PH}

The graphene coated cells have J_{SC} increases that are tied to how well they are covered by graphene, and their original uncoated J_{SC}. As is expected, cell G displays the

greatest increase in current characteristics as it originally had the worst resistance characteristics. The J_{SC} increases by 6 $\frac{mA}{cm^2}$, and is a representation of how effective the graphene is at mitigating the series resistance issues. This is a significant increase as it is of a magnitude similar to removing coverage compensation from cells like in chapter 2, as well as the increase between J_{PH} and J_{SC} after parasitic extraction as seen in the previous section.

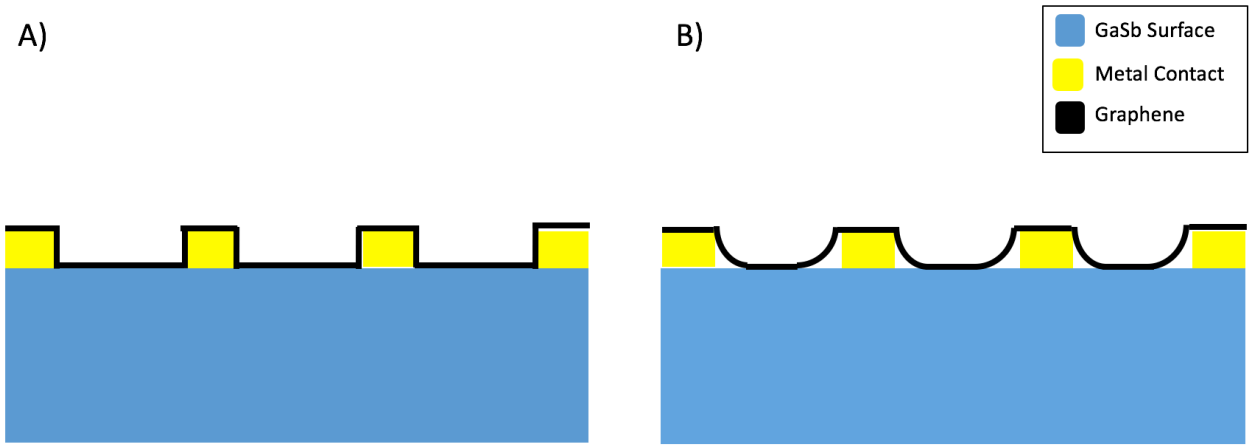

Figure 21 A & B: Fig 21 A is what a conformal coating should look like; the graphene coating covers all surfaces equally and is in complete contact with the semiconductor surface. Fig. 22 B is what the transferred graphene most likely looks like; the graphene hangs off of the metal surface and is in incomplete contact with the semiconductor surface

Examining the data for evidence of surface passivation in these cells is difficult, as the conformal coating of graphene to the surface of the exposed GaSb is not assured. It would be optimal to have a graphene coating that looks like that which is pictured in Figure 21. It is much more likely that coverage of the cells was similar to Figure 22, where the transferred graphene is not in contact with the semiconductor surface and it only has the capability to act as an aid to resistance characteristics, and not surface passivation. The best indication of surface passivation would be an increase in the

photocurrent of the devices, which occurred for two out of three of the tested devices. This would imply that the graphene is able to reduce the surface recombination velocity of GaSb in some cases since the layer does not act as an anti-reflection coating. On the contrary, it is thought to attenuate the incoming light across a broadband of wavelengths by about 3%. Also there can be process variation in the successful application of the graphene to the surface. The photocurrent in cell G goes down after graphene application by 2.2%, which could be the result of the known light absorption of graphene in the presence of no surface recombination velocity reduction. Cells D & E both had small increases in their photocurrent, but they were not as significant as the increase seen in J_{SC} observed after graphene application. These results cannot be seen as conclusive, as the graphene transferred onto these cells do not have conformal coverage. More work would need to be done in investigating the possibilities of graphene transfer as a transparent conductive electrode and surface passivation layer.

Chapter 4: Conclusion and Future work

Conclusions on the GaSb Parasitic Resistance Problem

When considering the operation of GaSb solar cells, the issue of solving the series and shunt resistance problems is difficult as they are tied directly into the cell production process as well as material growth characteristics. Series resistance problems stem from the large sheet resistance that exist in GaSb bulk and cannot be resolved without losing the long carrier lifetimes that make MBE growth worthwhile. This makes developing low resistance front contacts difficult for the devices difficult, and several solutions were attempted to optimize and improve the front metal contact grid. First an algorithm was developed to be able to create a front contact pattern that could have less total coverage area (10 % vs. 15 %) while still collecting the same amount of charge. This proved to be successful, but the resistance characteristics were still too poor to be an effective device. In removing the parasitic resistances from characterisitic photovoltaic equations, it was shown that the devices behaved better than their measure J_{SC} would indicate. Photocurrent's were calculated to be as much as 6 mA/cm^2 and were on the same magnitude as removing coverage area from device data. To solve the parasitic resistance issues, several solutions were tried.

Adding additional metal height to the front contact reduced these poor resistance values to consistent levels and made consistently larger J_{SC} values. The exception to this was devices with few fingers and large exposed semiconductor area as the sheet resistance of the emitter layer of GaSb was large. Graphene was proposed as an alternative to the additional metallization step, and single layer graphene was transferred

onto previously fabricate GaSb devices to assess its ability to reduce the characteristic resistance of the devices as well as potentially aid in surface passivation of the photovoltaics. The graphene proved to be effective in reducing the overall series resistance of the devices and increasing the shunt resistance. The change in these resistances would be useful in examining in terms of fill factor change. The fill factor change would add context to each of the resistance methods and allow for a comparison between each method directly. Additional studies into both graphene on GaSb technologies as well as full blackbody measurements will be necessary to fully understand these Thermo-photovoltaics.

Blackbody Cell Measurements

Though AM 1.5 measurements are easy to compare to other published results, it makes sense to test the devices under full TPV conditions. The most difficult aspect about testing devices under blackbody conditions is that the conditions for conducting these tests are not standardized. Most AM 1.5 simulators can be created to a degree of precision and standardization that cells tested under one simulator can except to have similar results when tested under a different one. Blackbody radiators can have variable heat sources, and are harder to shutter than their AM 1.5 counterparts as attempting to open and close a 900 K heat source can be a challenge.

The devices fabricated at Virginia Tech need to be tested under full TPV conditions, and until recent packaging issues were solved, this was considered an impossibility. The cells would be tested under the same voltage sweep as the AM 1.5 measurements with the a calibrated blackbody source to get measurements as consistently

as possible. These results will be worthwhile, especially for the graphene coated cells and the quaternary cells, as both possess properties which are not able to be assessed properly under AM 1.5.

Full Graphene Front Contacts

Using graphene as a complete front contact is the next logical step in its use in GaSb cell designs. By using graphene as a front metal contact, the coverage area tradeoff that is inherent to using metal as a front contact could be mitigated. Graphene also functions as a perfect barrier, meaning that metal deposited on top of it to make contact more efficient during testing would not have the same risk of physically touching the cell surface. This would make depositing metal easier as a thinner stack could be used with less risk of the metal remaining on the cell during deposition.

The transfer process of graphene is still a limiting factor in terms of how effective graphene could function as a front metal contact. It is an imprecise process and ability to coat the entire surface of a grown piece of MBE material could be a challenge. Patterning and depositing metal onto graphene without disrupting its periodicity is also difficult and these issues would need to be tested and addressed before using graphene as a front metal contact could be achieved.

Etching of Graphene Using CO_2

Though graphene stands a good chance of being incorporated into top down semiconductor processing techniques, the etching of graphene repeatedly is still an issue. At the nanoscale, graphene can display properties not seen in its bulk form. The reason

behind this difference is the edge states of graphene in these small size scales start to interfere with the band structures of graphene. The energy of the edge band states are strong enough that they can interact with each other across from the etched sample and depending on the type of edge created, will exhibit semi-conducting behavior.

CO_2 is a gas which in its plasma form can contain radical carbon and oxygen atoms. These carbon atoms could interact with the graphene during the etch process and give a more consistent etch result. Preliminarily, it has been shown that CO_2 can in fact etch graphene and leaves little residue in between etched patterns; a problem see in other etchant gases such as O_2. To understand if CO_2 had any real sort of impact on edge formation in the graphene devices, several tests would need to take place. First, the graphene would need to be etched into a hall bar pattern by both CO_2 and conventional O_2 gases, and their behavior would need to be examined. The etched surfaces would need to be compared by optical microscopy and well as AFM to attempt to get a better understanding of the topography of the sample. TEM is the best way to assess the edges of these graphene samples, and the etched samples would need to be processed so that TEM could attempt to look at how the edges formed after a CO_2 etch. To truly test if the CO_2 could provide a consistent edge type, the samples would need to be patterned via e-beam lithography into hall bars, then etched, to observe the quantum hall behavior of the samples. With the exception of the characterization of these samples, most of these steps have been completed, and repeated testing of the process and the samples is necessary to achieve conclusive resu

References

[1] "World population projected to reach 9.7 billion by 2050 | UN DESA | United Nations Department of Economic and Social Affairs." .

[2] "Detailed Balance Limit of Efficiency of p-n Junction Solar Cells," *J. Appl. Phys.*, vol. 32, no. 3, pp. 510–519, Mar. 1961.

[3] A.-E. Becquerel, *Mémoire sur les effets électriques produits sous l'influence des rayons solaires*. 1839.

[4] "This Month in Physics History." [Online]. Available: https://www.aps.org/publications/apsnews/200904/physicshistory.cfm. [Accessed: 22-Apr-2017].

[5] "Photovoltaic Research | NREL." [Online]. Available: https://www.nrel.gov/pv/. [Accessed: 22-Apr-2017].

[6] NREL, "Best Research-Cell Efficiencies." [Online]. Available: https://www.nrel.gov/pv/assets/images/efficiency-chart.png. [Accessed: 22-Apr-2017].

[7] H. F. Wolf, *Silicon semiconductor data*. Pergamon Press, 1969.

[8] "Principles of Photovoltaics, Photovoltaic Materials | Solar Energy." [Online]. Available: http://www.greenrhinoenergy.com/solar/technologies/pv_cells.php. [Accessed: 17-Apr-2017].

[9] B. Morgan *et al.*, "Power considerations for MAST platforms," 2010, vol. 7679, p. 76790V–76790V–12.

[10] D. K. Maurya, S. Das, and S. K. Lahiri, "Silicon MEMS vaporizing liquid microthruster with internal microheater," *J. Micromechanics Microengineering*, vol. 15, no. 5, pp. 966–970, May 2005.

[11] M. S. Shur, *Handbook Series on Semiconductor Parameters*. World Scientific, 1996.

[12] D. Martín and C. Algora, "Temperature-dependent GaSb material parameters for reliable thermophotovoltaic cell modelling," *Semicond. Sci. Technol.*, vol. 19, no. 8, p. 1040, 2004.

[13] "Part II – Photovoltaic Cell I-V Characterization Theory and LabVIEW Analysis Code - National Instruments." [Online]. Available: http://www.ni.com/white-paper/7230/en/. [Accessed: 20-Apr-2017].

[14] "Theory of solar cells," *Wikipedia*. 17-Mar-2017.

[15] D. R. Cooper *et al.*, "Experimental Review of Graphene," *ISRN Condens. Matter Phys.*, pp. 1–56, Jan. 2012.

[16] D. Qian, G. J. Wagner, W. K. Liu, M.-F. Yu, and R. S. Ruoff, "Mechanics of carbon nanotubes," *Appl. Mech. Rev.*, vol. 55, no. 6, pp. 495–533, Oct. 2002.

[17] D. L. Nika and A. A. Balandin, "Phonons and Thermal Transport in Graphene and Graphene-Based Materials," *ArXiv160600488 Cond-Mat*, Jun. 2016.

[18] K. S. Novoselov *et al.*, "Two-dimensional gas of massless Dirac fermions in graphene," *Nature*, vol. 438, no. 7065, pp. 197–200, Nov. 2005.

[19] A. A. Balandin *et al.*, "Superior Thermal Conductivity of Single-Layer Graphene," *Nano Lett.*, vol. 8, no. 3, pp. 902–907, Mar. 2008.

[20] E. Muñoz, J. Lu, and B. I. Yakobson, “Ballistic Thermal Conductance of Graphene Ribbons,” *Nano Lett.*, vol. 10, no. 5, pp. 1652–1656, May 2010.
[21] J. Martin *et al.*, “Observation of electron–hole puddles in graphene using a scanning single-electron transistor,” *Nat. Phys.*, vol. 4, no. 2, pp. 144–148, Feb. 2008.
[22] X. Li *et al.*, “Large-Area Synthesis of High-Quality and Uniform Graphene Films on Copper Foils,” *Science*, vol. 324, no. 5932, pp. 1312–1314, Jun. 2009.
[23] K. S. Novoselov *et al.*, “Electric Field Effect in Atomically Thin Carbon Films,” *Science*, vol. 306, no. 5696, pp. 666–669, 2004.
[24] S. Chen *et al.*, “Raman Measurements of Thermal Transport in Suspended Monolayer Graphene of Variable Sizes in Vacuum and Gaseous Environments,” *ACS Nano*, vol. 5, no. 1, pp. 321–328, Jan. 2011.
[25] “Air Properties.” [Online]. Available: http://www.engineeringtoolbox.com/air-properties-d_156.html. [Accessed: 30-Nov-2016].
[26] J. W. Suk *et al.*, “Transfer of CVD-Grown Monolayer Graphene onto Arbitrary Substrates,” *ACS Nano*, vol. 5, no. 9, pp. 6916–6924, Sep. 2011.
[27] V. E. Dorgan, A. Behnam, H. J. Conley, K. I. Bolotin, and E. Pop, “High-Field Electrical and Thermal Transport in Suspended Graphene,” *Nano Lett.*, vol. 13, no. 10, pp. 4581–4586, Oct. 2013.
[28] L. Banszerus *et al.*, “Ultrahigh-mobility graphene devices from chemical vapor deposition on reusable copper,” *Sci. Adv.*, vol. 1, no. 6, p. e1500222, Jul. 2015.
[29] W. Cai *et al.*, “Thermal Transport in Suspended and Supported Monolayer Graphene Grown by Chemical Vapor Deposition,” *Nano Lett.*, vol. 10, no. 5, pp. 1645–1651, May 2010.
[30] L. Banszerus *et al.*, “Ballistic Transport Exceeding 28 μm in CVD Grown Graphene,” *Nano Lett.*, vol. 16, no. 2, pp. 1387–1391, Feb. 2016.
[31] D. A. Neamen, *Semiconductor Physics and Devices*, 4th ed. McGraw-Hill Education, 2003.
[32] N. Rahimi, “DESIGN, FABRICATION AND CHARACTERIZATION OF EPITAXIAL AND NON-EPITAXIAL THERMO-PHOTOVOLTAIC CELLS,” Jul. 2014.
[33] S. A. Abdallah, D. J. Herrera, B. P. Conlon, N. Rahimi, and L. F. Lester, “Emitter thickness optimization for GaSb thermophotovoltaic cells grown by molecular beam epitaxy,” 2015, vol. 9562, p. 95620L–95620L–7.
[34] L. M. Fraas, J. E. Avery, P. E. Gruenbaum, V. S. Sundaram, K. Emery, and R. Matson, “Fundamental characterization studies of GaSb solar cells,” in *, Conference Record of the Twenty Second IEEE Photovoltaic Specialists Conference, 1991*, 1991, pp. 80–84 vol.1.
[35] N. Rahimi *et al.*, “GaSb thermophotovoltaics: current challenges and solutions,” 2015, vol. 9358, pp. 935816-935816–10.
[36] “Electrical resistance and conductance,” *Wikipedia*. 05-Apr-2017.
[37] B.-C. Juang *et al.*, “GaSb thermophotovoltaic cells grown on GaAs by molecular beam epitaxy using interfacial misfit arrays,” *Appl. Phys. Lett.*, vol. 106, no. 11, p. 111101, Mar. 2015.

[38] R. R. Nair *et al.*, “Fine Structure Constant Defines Visual Transparency of Graphene,” *Science*, vol. 320, no. 5881, pp. 1308–1308, Jun. 2008.
[39] A. Reina *et al.*, “Large area, few-layer graphene films on arbitrary substrates by chemical vapor deposition,” *Nano Lett.*, vol. 9, no. 1, pp. 30–35, 2008.

Appendix A: RTA Chart

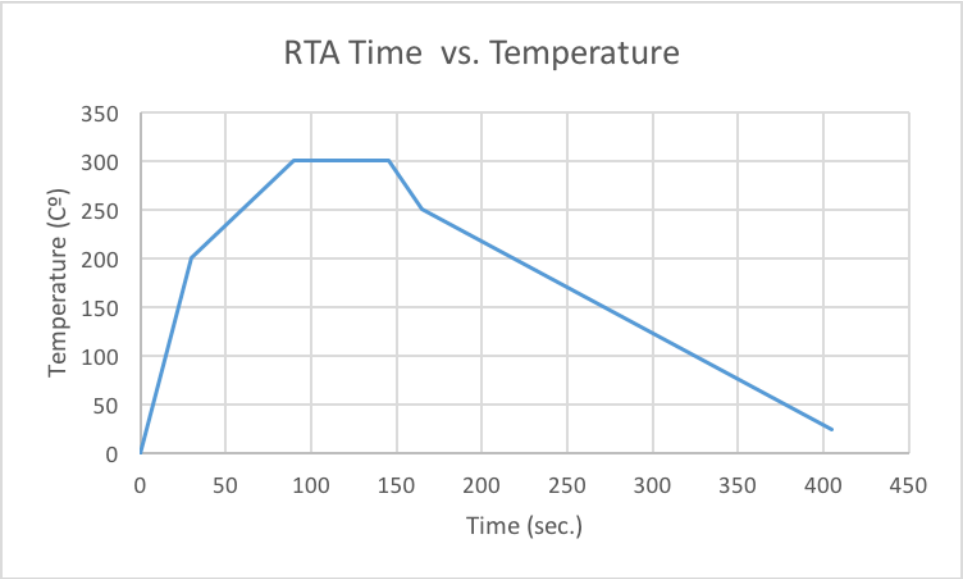

Appendix B: Full results

Wafer	Location (Block, Cell)	Voc (V)	Isc (A)	Jsc (mA/cm2)	Imax (A)	Vmax (V)	Pmax (mW)	Fill Factor (%)	Efficiency (%)	Rs at Voc (Ohm)	Rsh at Isc (Ohm)	Coverage Area	Jsc (mA/cm2)	n	Rseries (Ohm)	Rshunt (Ohm)	Io (Amp)	Iph (Amp)	JPH (mA/cm2)
GaSb (one metalization)	B1 C1	0.2064	0.0090804	36.35369	0.0067267	0.1944105	0.9041452	48.1982	3.6166	6.623213	104.588	0.152	42.8699175	1.1	3.48845	101.0995545	5.2659E-06	0.009413	44.39988324
GaSb (one metalization)	B1 C2	0.20338	0.0087122	34.848864	0.0058506	0.1214927	0.7107995	40.11477	2.8432	10.700192	81.776	0.0987	38.6651104	1.1	7.43007	74.3459274	5.4771E-06	0.009631	42.74076194
GaSb (one metalization)	B1 C3	0.19749	0.0066538	26.613552	0.0042761	0.1840449	0.5063125	38.53044	2.0252	12.872326	95.599	0.162	31.7605632	1.1	8.59059	87.10894121	4.9569E-06	0.007943	35.04866496
GaSb (one metalization)	B1 C4	0.20356	0.0087851	35.140472	0.0067324	0.1451137	0.9765587	54.6307	3.9078	4.480758	610.352	0.144	41.0519533	1.1	1.23777	609.114226	6.6882E-06	0.008806	41.14990847
GaSb (one metalization)	B1 C5	0.20021	0.0083293	32.917228	0.0062085	0.1410169	0.8755038	53.1392	3.502	5.507045	254.816	0.0978	36.485511	1.1	2.04503	252.770971	6.6692E-06	0.008301	36.80451874
GaSb (one metalization)	B1 C6	0.1941	0.0062995	25.19812	0.0037649	0.1159479	0.4361589	35.6711	1.7446	14.724915	76.7	0.098	27.9358315	1.1	10.20224	66.49764446	4.8307E-06	0.007307	32.40489224
GaSb (one metalization)	B2 C1	0.20453	0.0054966	21.986442	0.0032182	0.1188145	0.3823704	34.0118	1.5294	19.718218	81.488	0.152	25.927408	1.1	14.535	66.9529767	2.8066E-06	0.006733	31.76146222
GaSb (one metalization)	B2 C2	0.20105	0.0053675	21.470168	0.0031995	0.1154714	0.3694448	34.4347	1.4778	21.349093	84.327	0.0987	23.8213336	1.1	16.04413	68.28573869	3.2308E-06	0.006692	29.69739791
GaSb (one metalization)	B2 C3	0.1912	0.0047709	19.083456	0.0029304	0.1083084	0.3168048	34.7311	1.2672	22.885315	98.629	0.162	22.7726205	1.1	16.91361	81.71535947	4.125E-06	0.005826	27.81040318
GaSb (one metalization)	B2 C4	0.20533	0.0068844	27.537674	0.0043972	0.1156958	0.5087319	35.9548	2.035	17.198083	77.387	0.144	32.1701799	1.1	13.06598	64.32724467	3.8113E-06	0.008368	39.10161231
GaSb (one metalization)	B2 C5	0.18954	0.0057607	23.042748	0.0030258	0.101176	0.3061392	28.0376	1.2246	25.412265	47.614	0.0978	25.5406207	1.1	20.4667	27.1473231	4.3824E-06	0.010374	45.59484948
GaSb (one metalization)	B2 C6	0.18892	0.0041972	16.78861	0.0022428	0.1034572	0.2320347	29.3624	0.9282	31.113627	60.289	0.098	18.6126497	1.1	24.3257	35.96333124	2.4678E-06	0.007123	31.58537283
GaSb (two metalization)	B1 C1.1	0.21154	0.0103802	41.52096	0.0081749	0.1512249	1.2362518	56.2995	4.945	4.094416	638.57	0.152	48.9633962	1.1	1.34978	637.220222	6.0088E-06	0.010406	49.08511652
GaSb (two metalization)	B2 C2	0.21004	0.0094437	37.774892	0.0074712	0.1482304	1.1074628	55.8323	4.4299	4.510871	252.27	0.0987	41.9115633	1.1	1.49405	250.7759949	5.4488E-06	0.009303	42.17674519
GaSb (two metalization)	B2 C3	0.20315	0.0077275	30.90999	0.0060398	0.1469836	0.8877568	56.5501	3.551	5.23249	193.765	0.162	36.8854296	1.1	1.54586	192.219143	5.3941E-06	0.007792	37.19545085
GaSb (two metalization)	B2 C4	0.20987	0.0093935	37.17405	0.0072989	0.1517449	1.1075679	56.7871	4.4303	4.234092	531.152	0.144	43.4276285	1.1	1.16851	529.983488	5.6433E-06	0.009317	43.33560327
GaSb (two metalization)	B2 C5	0.2081	0.0086586	34.422332	0.0068187	0.1496886	1.0205501	56.9874	4.0822	4.391409	1109.878	0.0978	38.1537708	1.1	1.08077	1108.79723	5.6728E-06	0.008616	38.20065597
GaSb (two metalization)	B2 C6	0.20043	0.0075608	30.243946	0.00471	0.1237333	0.5827852	38.4572	2.3311	10.071054	88.246	0.0988	33.5292084	1.1	6.30295	81.94630458	5.0391E-06	0.008164	36.21493283

Appendix C: PV Characteristics Derivation

Looking at the circuit diagram of the PV device, to be able to extract the parasitic resistances from the cell behavior, we must make certain assumptions about the resistance behavior of the PN junction diode behavior. We must be able to say that the resistance across the diode is:

$$R_{diode} = \frac{dV}{dI} = \frac{nV_{th}}{I_{Diode}} \qquad \textit{Equation 7}$$

where I_{Diode} is the current which flows across the diode. At V_{OC} we can use these assumptions to say that the resistance of the current passing through the PN diode is significantly smaller than R_P and thus R_{Diode} dominates their parallel relationship. If we assume that this resistance is parasitic and shows up in the measured resistances results, we can find more accurate resistances of the device at points calculated from cell data. Using the knowledge that series resistance effects the measured resistance at V_{OC}, we can subtract the diode resistance from the measured resistance to arrive at the true series resistance of the device. We use the short circuit current of the device as the current passing through the diode as it is a physically measured value that can represent in these circumstances the photogenerated current of the device. This gives rise to equation 8:

$$R_{Series} = R@V_{OC} - \frac{nV_{th}}{I_{sc}} \qquad \textit{Equation 8}$$

Following the same line of thinking, at I_{SC} the resistance measured will include the shunt resistance as well as the series resistance (which is parasitic to the measured value). This allows us to arrive at equation 9 for the shunt resistance:

$$R_P = R@I_{SC} - R_S \qquad \textit{Equation 9}$$

Now that we have established the actual series and shunt resistances of the device, we can examine the single diode model of equation 4 in more detail.

$$I = I_{PH} - I_0 \left[\exp\left(\frac{V+IR_S}{nV_{th}}\right) - 1\right] - \left(\frac{V+IR_S}{R_p}\right) \qquad \textit{Equation 4}$$

This equation can be reduced when examined at V_{OC} and I_{SC};

@ V_{OC}

$$0 = I_{PH} - I_0 \left[\exp\left(\frac{V+(0)R_s}{nV_{th}}\right) - 1\right] - \left(\frac{V+(0)R_s}{R_p}\right)$$

$$-I_{PH} = -I_0 \left[\exp\left(\frac{V+(0)R_s}{nV_{th}}\right) - 1\right] - \left(\frac{V+(0)R_s}{R_p}\right)$$

Normalizing this expression to positive signs gives us Equation 5, a transcendental that is possible to be solved now that R_P is known.

$$I_{ph}=I_0\left[\exp\left(\frac{V_{OC}}{nV_{th}}\right)-1\right]+\left(\frac{V_{OC}}{R_{Shunt}}\right) \qquad I_{ph}=I_0\left[\exp\left(\frac{V_{OC}}{nV_{th}}\right)\text{-}1\right]+\left(\frac{V_{OC}}{R_p}\right)$$

Equation 5

Examining the Equation 4 at I_{SC} we can arrive at Equation 6
@I_{SC}

$$I_{SC}=I_{PH}\text{-}I_0\left[\exp\left(\frac{(0)+I_{SC}R_S}{nV_{th}}\right)\text{-}1\right]\text{-}\left(\frac{(0)+I_{SC}R_S}{R_p}\right)$$

$$I_{SC}=I_{PH}\text{-}I_0\left[\exp\left(\frac{I_{SC}R_S}{nV_{th}}\right)\text{-}1\right]\text{-}\left(\frac{I_{SC}R_S}{R_p}\right) \qquad \textit{Equation 6}$$

Because of the assumptions made about device operation, we can use the calculated R_S and R_P create a system of equations in which we find I_0 and I_{PH}.

Sub Equation 5 into Equation 6 to attempt to find I_0:

$$I_{SC}=I_0\left[\exp\left(\frac{V_{OC}}{nV_{th}}\right)\text{-}1\right]+\left(\frac{V_{OC}}{R_{Shunt}}\right)\text{-}I_0\left[\exp\left(\frac{I_{SC}R_S}{nV_{th}}\right)\text{-}1\right]\text{-}\left(\frac{I_{SC}R_S}{R_p}\right)$$

$$I_{SC}\text{-}\left(\frac{V_{OC}}{R_P}\right)+\left(\frac{I_{SC}R_S}{R_p}\right)=I_0\left[\exp\left(\frac{V_{OC}}{nV_{th}}\right)-1\right]\text{-}I_0\left[\exp\left(\frac{I_{SC}R_S}{nV_{th}}\right)-1\right]$$

$$I_{SC}*\left(1+\frac{R_S}{R_p}\right)\left(\frac{V_{OC}}{R_P}\right)=I_0\left(\left[\exp\left(\frac{V_{OC}}{nV_{th}}\right)-1\right]\left[\exp\left(\frac{I_{SC}R_S}{nV_{th}}\right)-1\right]\right)$$

Which reduces to equation 10

$$I_0=\left[\frac{I_{SC}*\left(1+\frac{R_{Series}}{R_{Shunt}}\right)\text{-}\left(\frac{V_{OC}}{R_{Shunt}}\right)}{\frac{1}{\exp\left(\frac{V_{OC}}{V_{th}*n}\right)}\text{-}\exp\left(\frac{I_{SC}*R_{Series}}{V_{th}*n}\right)}\right]$$

$$I_0=\left[\exp^{-1}\left(\frac{V_{OC}}{V_{th}*n}\right)*\exp\left(\frac{I_{SC}*R_{Series}}{V_{th}*n}\right)\right]^{-1}*\left[I_{SC}*\left(1+\frac{R_{Series}}{R_{Shunt}}\right)\text{-}\left(\frac{V_{OC}}{R_{Shunt}}\right)\right] \qquad \textit{Equation 10}$$

Using this value we can calculate an exact value of I_{PH} as shown in Equation 11

$$I_{ph}=I_0\left[\exp\left(\frac{V_{OC}}{nV_{th}}\right)-1\right]+\frac{V_{OC}}{R_{Shunt}}$$

$$I_{ph}=I_0\left[\exp\left(\frac{V_{OC}}{nV_{th}}\right)-1\right]+\frac{V_{OC}}{R_{Shunt}} \qquad \textit{Equation 11}$$